THE ASTROPHYSICAL JOURNAL, 470:249–268, 1996 October 10


# THE TWO-PHASE PAIR CORONA MODEL FOR ACTIVE GALACTIC NUCLEI AND X-RAY BINARIES: HOW TO OBTAIN EXACT SOLUTIONS

JURI POUTANEN AND ROLAND SVENSSON
Stockholm Observatory, S-133 36 Saltsjöbaden, Sweden; juri@astro.su.se, svensson@astro.su.se
*Received 1995 November 22; accepted 1996 April 30*

## ABSTRACT

We consider two-phase accretion disk–corona models for active galactic nuclei and some X-ray binaries. We describe in detail how one can exactly solve the polarized radiative transfer and Comptonization by using the iterative scattering method while simultaneously solving the energy and pair balance equation for both the cold and hot phases. We take into account Compton scattering, photon-photon pair production, pair annihilation, bremsstrahlung, and double Compton scattering, as well as exact reflection from the cold disk. We consider coronae with slab geometry, as well as coronae consisting of one or more well-separated active regions of cylindrical or hemispheric geometry. The method is useful for determining the spectral intensity and the polarization emerging in different directions from disk-corona systems. The code is tested against a Monte Carlo code. We also compare with earlier, less accurate, work. The method is more than an order of magnitude faster than applying Monte Carlo methods to the same problem and has the potential of being used in spectral fitting software, such as XSPEC.

*Subject headings:* accretion, accretion disks — galaxies: active — methods: numerical — polarization — scattering — X-rays: general

## 1. INTRODUCTION

Both active galactic nuclei (AGNs) and certain X-ray binaries (the Galactic black hole candidates, GBHCs) show X-ray spectra that extend into the hard X-rays (see, e.g., Mushotzky, Done, & Pounds 1993; Tanaka & Lewin 1995). The X-ray spectra of Seyfert 1 galaxies show at least two components: (1) an intrinsic power-law component with an intensity index $\alpha \sim 0.9$–$1.0$ in the 2–18 keV range and a spectral cutoff at a few hundred keV (Zdziarski et al. 1994; Madejski et al. 1995; Zdziarski et al. 1995) and (2) a superposed reflection component that arises from reflection and reprocessing of the intrinsic power law by cold, opaque matter subtending $\sim(1$–$2)\pi$ sr solid angle as viewed from the X-ray source (see, e.g., Nandra & Pounds 1994). GBHCs such as Cyg X-1 and 1E 1740.7−2942 show power-law spectra that extend up to hundreds of keV (see, e.g., Gilfanov et al. 1994; Tanaka & Lewin 1995). The characteristic features of reflection have been seen in GBHCs as well (e.g., Done et al. 1992).

AGNs and GBHCs are believed to be powered by accretion through an accretion disk. In the unified model for AGNs (see, e.g., Antonucci 1993), it is believed that we are viewing the disks in Seyfert 1 galaxies more or less face-on while, for Seyfert 2 galaxies, we are viewing the disk more or less edge-on through a molecular torus. In GBHC sources, we are viewing the binary system along some given (possibly time dependent) direction. The X-ray spectra indicate the existence of both hot X-ray–emitting and cold reflecting gas components. The exact geometry is not known, but a currently popular model is the two-phase disk-corona model (see, e.g., Haardt & Maraschi 1991, 1993, hereafter HM93). The blackbody disk radiation from the cold disk (in the EUV for AGNs, and in soft X-rays for GBHCs) enters the hot corona from one side and is Comptonized into X-rays. Part of this X-ray radiation is incident on the cold disk and is partly reflected but mainly reprocessed into soft blackbody radiation. The remaining part forms the X-ray spectrum that leaves the disk-corona system. Both the blackbody and the Comptonized spectra are anisotropic, so observers at different viewing angles see different spectra (HM93). It immediately clear that such models are neither homogeneous nor spherically symmetric. In order to correctly interpret observed X-ray spectra of AGNs and GBHCs, one needs to know the theoretical spectra for mildly relativistic temperatures and for different viewing angles.

Theoretical Comptonized spectra have been computed for two decades now. Almost all works make simplifying assumptions that render them useless for interpreting X-ray spectra from sources for which anisotropic effects are important. We briefly discuss standard methods for modeling Comptonized spectra from AGNs and GBHCs at mildly relativistic temperatures.

One approach is to treat the photon- and pair-producing processes, as well as the energy and pair balance, in great detail but to make large simplifications regarding the radiative transfer, using various prescriptions for the spectral shape and simple escape probabilities to obtain the photon density (e.g., Zdziarski 1985; Pietrini & Krolik 1995). Such calculations can only yield very approximate relations between the typical spectral shape and other parameters.

Other approaches are to compute detailed radiative transfer by using Monte Carlo methods for geometries such as slabs or spheres (e.g., Hua & Titarchuk 1995) or to improve the analytic theory of Comptonization (e.g., Titarchuk 1994). Normally, the following simplifications are made: (1) processes other than Comptonization are neglected, (2) pair balance is not imposed, (3) angle dependence of output spectra is not considered, and (4) the soft photon injection is homogeneous throughout the source. There are some exceptions. For example, Skibo et al. (1995) included bremsstrahlung, pair production, and pair balance, and Zdziarski et al. (1994) assumed the soft photons to be injected at one of the slab surfaces. Most works neglect

reflection by cold matter. The few papers that consider polarized radiative transfer (e.g., Sunyaev & Titarchuk 1985; Haardt & Matt 1993) have used the Rayleigh matrix, which is not valid for temperatures and photon energies above 50 keV.

Pioneering steps were taken by Haardt & Maraschi (1991, 1993) and Haardt (1993, 1994) to solve for angle-dependent spectra from disk-corona systems including reflection as well as energy and pair balance. The method treated the first scattering order accurately but assumed higher order scatterings to be isotropic. Compton recoil was neglected, and therefore the spectral cutoff at photon energies around and above $kT_e$ could not be treated. Furthermore, the pair balance treatment was approximate, as they adopted the semianalytical theory of Zdziarski (1985), using prescribed spectra. Finally, when determining the reflected spectrum, they assumed the X-ray flux incident on the cold matter to be isotropic. Further steps were taken by Stern et al. (1995a, 1995b), who used nonlinear Monte Carlo techniques to treat disk-corona systems with different inhomogeneous coronal geometries. Here exact pair balance was imposed throughout the coronal region. Furthermore, output spectra (including the cutoff) had sufficiently good statistics to allow the dependence on the viewing angle to be studied. These works found that anisotropic effects are very important for spectra from disk-corona systems. At mildly relativistic temperatures, the first-order scattering of the soft disk radiation is suppressed in the face-on direction. This causes the face-on spectrum to be harder up to the spectral peak of the second-order scattering, where an *anisotropy break* appears. Above the break, the Comptonized spectrum in all directions resembles the angle-averaged one. As shown in Stern et al. (1995b), the anisotropy break easily appears in the 2–18 keV range, making $\alpha_{2-18}$ strongly dependent on viewing angle. The reflection component is also strongly anisotropic (see, e.g., Matt 1993; Magdziarz & Zdziarski 1995; Poutanen, Nagendra, & Svensson 1996).

The disadvantage of the nonlinear Monte Carlo method is that it is computer intensive, requiring more than 1 hour per run on a SPARC 20. In order to be able to perform spectral fitting of observed spectra, one needs a much faster method to compute accurate angle-dependent spectra from disk-corona systems. In the present paper, we describe such a fast code that is based on the iterative scattering method, i.e., in which the radiative transfer equation is solved for each scattering order (see, e.g., Sunyaev & Titarchuk 1985). Most important radiation processes are included. Energy and pair balance can be imposed. The reflection is accurately treated, accounting for the full angular dependence of the incident spectrum (Poutanen et al. 1996). Slab, cylindrical, and hemispheric geometries of the corona can be treated. Finally, the radiative transfer is polarized as regards both the Comptonization and the reflection. The code has already been used to interpret the statistics of observed X-ray spectral indices and compactnesses from Seyfert 1 galaxies (Stern et al. 1995b). The purpose of the present paper is to fully document the methods used in the code in a self-contained way.

In the remainder of this paper, we first describe the setup of the two-phase disk-corona model in § 2. The methods of solving the radiative transfer equation in different geometries are considered in § 3. The energy and pair balance and details of the iteration procedure are considered in § 4. We compare our results with those of other available codes in § 5, where we also consider the accuracy and efficiency of various approximations that can be employed in order to decrease the computing time. Finally, we summarize our work in § 6. Expressions for the reaction rates and redistribution functions (i.e., the Compton redistribution matrix) are given in the Appendix.

## 2. SETUP

We consider the simple two-phase disk-corona model, in which a hot corona is located above an optically thick plane-parallel cold slab ("disk"; see, e.g., Haardt & Maraschi 1991, 1993; Haardt, Maraschi, & Ghisellini 1994). The hot corona is either a plane-parallel slab (with vertical thickness $H$) or an active region with the shape of a hemisphere (with radius $R$) or a cylinder (with vertical height $H$ and horizontal radius $R$). We allow energy dissipation in both the corona and the cold disk. The radiation escaping from the cold disk consists of a soft component and a reflected component. The soft flux is equal to the sum of the absorbed incident flux from the corona and the flux due to local energy dissipation in the cold disk. The spectral shape of these soft components is assumed to be Planckian, with temperatures $T_{\rm bb}$ and $T_{\rm disk}$, respectively (note that $T_{\rm bb} > T_{\rm disk}$). The shape of the reflected component is determined by the shape of incident coronal X-ray radiation (mainly resulting from Comptonization of the soft disk radiation) and the effects of photoelectric absorption and Compton scattering in the cold disk (see, e.g., White, Lightman, & Zdziarski 1988; Magdziarz & Zdziarski 1995).

We can treat coronae either with or without pairs. In this paper, we mostly consider the case of a pure pair corona without any background plasma. The pure pair corona is a consequence of photon-photon pair production above the cold disk. The electrons and positrons are assumed to have a relativistic Maxwellian distribution of the same temperature, $\Theta = kT_e/m_e c^2$. The corona is assumed to be uniform in temperature and pair density, and pair escape is neglected. If all power is dissipated in the corona, then, for a given geometry, the two parameters, the total power dissipated in the corona, $L_{\rm diss}$, and the temperature, $T_{\rm bb}$, of the reprocessed radiation, uniquely determine the optical depth, $\tau_{\rm T}$, and the coronal temperature, $\Theta$. If the radiation produced internally in the disk is nonnegligible, then two more parameters are important: the disk temperature, $T_{\rm disk}$, and the ratio $d = L_{\rm disk}/L_{\rm diss}$, where $L_{\rm disk}$ is the luminosity that is produced internally in the disk and that enters the corona. For all geometries, $\tau_{\rm T}$ is defined as the total vertical Thomson optical depth of the corona (along the symmetry axis in the case of hemispheric geometry).

To solve the pair balance equation, the energy balance equations for the cold and hot phases, and the radiative transfer in the corona self-consistently, we make use of an iteration procedure. To reduce computing time, we chose to fix $\Theta$, which allows us to compute the thermal Compton redistribution matrix and cross section and the coronal emissivities for pair annihilation and bremsstrahlung before doing the iterations. We then adjust $\tau_{\rm T}$ and $L_{\rm diss}$ until the radiation spectra from solving the radiative transfer satisfy the energy balance equations and the pair balance.

When solving the radiative transfer/Comptonization problem, we account for the angular anisotropy of the radiation as well as its polarization properties. The reprocessing in the cold disk is described by Green's matrix (consisting of four Green's functions) for reflection, where we fully account for the Compton effect, photoelectric absorption, and iron fluorescence, as

well as for the angular and polarization properties of the radiation incident on the cold disk (Poutanen et al. 1996). We reduce the time needed to compute the reflection spectrum substantially by using a precalculated Green's matrix and achieve better accuracy than all previous treatments of the problem (e.g., White et al. 1988; Magdziarz & Zdziarski 1995).

As additional photon sources and cooling processes of the corona, we consider electron-electron, positron-positron, and electron-positron bremsstrahlung, double Compton scattering, and pair annihilation. We also account for photon absorption due to pair production, which can be important in determining the spectral shapes at pair-producing energies ($h\nu > m_e c^2$) and, thus, in influencing the pair balance.

The radiative transfer equation is solved by expanding the radiation field in scattering orders (the iterative scattering method; see, e.g., Sunyaev & Titarchuk 1985). The intensity in a slab-corona is a function of vertical position (i.e., the Thomson optical depth variable, $\tau$), zenith angle, and frequency but is independent of azimuth. In an active region, the intensity of course depends on the distance from the symmetry axis and the azimuth angle, making the spatial part of the problem two-dimensional. However, by averaging the radiation field over horizontal layers in the active region, we convert the two-dimensional problem into a one-dimensional problem suitable for our one-dimensional code. We discuss the accuracy of this conversion in § 5.

In the pair balance, we use a volume-averaged pair production rate. In the energy balance equations, we need the total luminosities emerging from the cold and hot phases. Therefore we compute and sum the radiative fluxes emerging from all surfaces of the disk and the corona, accounting for all radiative transfer effects.

## 3. RADIATIVE TRANSFER

### 3.1. *Radiative Transfer in a Slab-Corona*

As a result of azimuthal symmetry and the absence of sources of circular polarization, the radiation field and the degree of polarization at a vertical position $z$ can be fully described by a Stokes vector consisting of two Stokes parameters (Chandrasekhar 1960), $\boldsymbol{I} = \boldsymbol{I}(z, x, \mu) = (I, Q)^T$, where superscript $T$ denotes the transposed vector. The radiative transfer equation describing the propagation of polarized light through a plane-parallel electron (and positron) atmosphere in steady state can be written in the following form:

$$\mu \frac{d\boldsymbol{I}(z, x, \mu)}{dz} = -[n_e \sigma_{\rm CS}(x) + \alpha_{\gamma\gamma}(z, x, \mu)]\boldsymbol{I}(z, x, \mu) + n_e \sigma_{\rm T} \boldsymbol{S}(z, x, \mu) + \epsilon(x)\begin{pmatrix}1\\0\end{pmatrix}, \tag{1}$$

where $x \equiv h\nu/m_e c^2$ is the photon energy, $n_e = n_+ + n_-$ is the total electron and positron density, $\mu$ is the cosine angle between the slab normal and the direction of photon propagation, $\sigma_{\rm CS}(x)$ cm$^2$ is the thermal Compton scattering cross section, $\sigma_{\rm T}$ cm$^2$ is the Thomson cross section, $\alpha_{\gamma\gamma}(z, x, \mu)$ cm$^{-1}$ is the absorption coefficient due to photon-photon pair production, and $\boldsymbol{S}(z, x, \mu)$ is the electron scattering source function. The emissivity, $\epsilon(x) = \epsilon_{++} + \epsilon_{--} + \epsilon_{+-} + \epsilon_{\rm ann} + \epsilon_{\rm DC}$ ergs cm$^{-1}$ s$^{-1}$ sr$^{-1}$, which is assumed to be isotropic and homogeneous, includes all photon sources in the atmosphere, in our case electron-electron, positron-positron, and electron-positron bremsstrahlung, annihilation, and double Compton radiation. The expressions for the emissivities and absorption coefficients are given in the Appendix.

Using the following notation for the dimensionless intensity, source function, emissivities, scattering cross section, and absorption coefficient,

$$I' = I\frac{H\sigma_{\rm T}}{m_e c^3}, \qquad S' = S\frac{H\sigma_{\rm T}}{m_e c^3}, \qquad \epsilon' = \epsilon\frac{H}{n_e m_e c^3}, \qquad \sigma'_{\rm CS} = \frac{\sigma_{\rm CS}}{\sigma_{\rm T}}, \qquad \alpha'_{\gamma\gamma} = \frac{\alpha_{\gamma\gamma}}{n_e \sigma_{\rm T}},$$

and removing the primes, the radiative transfer equation can be written in the following dimensionless form:

$$\mu \frac{d\boldsymbol{I}(\tau, x, \mu)}{d\tau} = -[\sigma_{\rm CS}(x) + \alpha_{\gamma\gamma}(\tau, x, \mu)]\boldsymbol{I}(\tau, x, \mu) + \boldsymbol{S}(\tau, x, \mu) + \epsilon(x)\begin{pmatrix}1\\0\end{pmatrix}, \tag{2}$$

where $d\tau = \sigma_{\rm T} n_e dz$ is the differential Thomson optical depth. Hereafter we will only use dimensionless quantities (except in the Appendix).

The Thomson optical depth of the slab is $\tau_{\rm T} = H\sigma_{\rm T} n_e$. The boundary conditions at the upper and lower surface of the slab are

$$\boldsymbol{I}(\tau = \tau_{\rm T}, x, -\mu) = 0 \quad (\mu > 0), \qquad \boldsymbol{I}(\tau = 0, x, \mu) = \boldsymbol{I}_{\rm in}(x, \mu), \tag{3}$$

i.e., there is no radiation incident at the upper surface, and the radiation incident at the lower surface consists of a reflected component, a soft reprocessed component, and a soft component internally produced in the disk:

$$\boldsymbol{I}_{\rm in}(x, \mu) = \boldsymbol{I}_{\rm refl}(x, \mu) + c_{\rm bb} B_x(T_{\rm bb})(1 \quad 0)^T + c_{\rm disk} B_x(T_{\rm disk})(1 \quad 0)^T. \tag{4}$$

The reflected radiation, $\boldsymbol{I}_{\rm refl}(x, \mu)$, from the cold disk can be found as a convolution of a reflection matrix (Green's matrix) $\mathbf{G}(x, \mu; x_1, \mu_1)$ with the incident radiation:

$$\boldsymbol{I}_{\rm refl}(x, \mu) = \int_x^\infty dx_1 \int_0^1 d\mu_1 \mathbf{G}(x, \mu; x_1, \mu_1)\boldsymbol{I}(\tau = 0, x_1, -\mu_1). \tag{5}$$

The Green's matrix maps incoming radiation at $(x_1, -\mu_1)$ into reflected radiation at $(x, \mu)$. To compute Green's matrix, we use the method developed by Poutanen et al. (1996). The normalization constants in front of the Planckian functions in equation (4) are determined by normalizing the blackbody flux to the soft compactnesses, $l_{\rm repr}$ and $l_{\rm disk}$ (to be defined in § 4.1),

as

$$c_{\rm bb}\pi\int_0^\infty dx\,B_x(T_{\rm bb}) = l_{\rm repr}\,, \qquad c_{\rm disk}\pi\int_0^\infty dx\,B_x(T_{\rm disk}) = l_{\rm disk}\,. \tag{6}$$

The thermal electron scattering source function, $S(\tau, x, \mu)$, can be expressed in terms of the azimuth-averaged Compton redistribution matrix (see, e.g., Poutanen & Vilhu 1993):

$$S(\tau, x, \mu) = x^2\int_0^\infty \frac{dx_1}{x_1^2}\int_{-1}^1 d\mu_1\begin{pmatrix} R_{11} & R_{12} \\ R_{21} & R_{22}\end{pmatrix} I(\tau, x_1, \mu_1)\,, \tag{7}$$

or, in operator form,

$$S = \mathbf{R}I\,. \tag{8}$$

The factor $x^2/x_1^2$ in equation (7) appears because we use the photon intensity instead of the photon occupation number to describe the radiation field (see Nagirner & Poutanen 1994). Expressions for the redistribution functions $R$ are given in the Appendix (§ A1).

We solve the integrodifferential equation (2) by expanding the Stokes vector $I$ in scattering orders (Neumann series):

$$I = \sum_{k=0}^{\infty} I_k\,, \tag{9}$$

where $I_k$ is the Stokes vector for photons having undergone $k$ scatterings (see, e.g., Sunyaev & Titarchuk 1985). This expansion converges quickly for sufficiently small optical depths ($\tau_{\rm T} \lesssim 1$). The source function for the nonscattered component consists of the flux incident on the corona at the bottom surface, $\tau = 0$, and the internal coronal sources:

$$S_0(\tau, x, \mu) = \mu I_{\rm in}(x, \mu)H(\mu)\delta(\tau) + \epsilon(x)(1 \quad 0)^T\,, \tag{10}$$

where $H(\mu)$ is the Heaviside function. The Stokes vectors, $I_k^{\pm}(\tau, x, \mu) = I_k(\tau, x, \pm\mu)$, for the upward and downward radiation and for all scattering orders $k \geq 0$ are calculated by employing the iteration formulae

$$I_k^+(\tau, x, \mu) = \int_0^\tau \frac{d\tau'}{\mu}\,S_k(\tau', x, \mu)\exp\left[-\int_{\tau'}^\tau \sigma(\tau'', x, \mu)\frac{d\tau''}{\mu}\right], \tag{11}$$

$$I_k^-(\tau, x, \mu) = \int_\tau^{\tau_{\rm T}} \frac{d\tau'}{\mu}\,S_k(\tau', x, -\mu)\exp\left[-\int_\tau^{\tau'} \sigma(\tau'', x, -\mu)\frac{d\tau''}{\mu}\right], \tag{12}$$

where $\sigma(\tau, x, \mu) = \sigma_{\rm CS}(x) + \alpha_{\gamma\gamma}(\tau, x, \mu)$. Using equation (8), the source function can be written as

$$S_{k+1} = \mathbf{R}I_k\,. \tag{13}$$

This procedure yields the dependence of the Stokes parameters on frequency, angle, and optical depth. Iterative methods in which the calculations of the spectral structure and of the angular polarization structure of the radiation field are separated (Sunyaev & Titarchuk 1985; Phillips & Mészáros 1986) fail to obtain the frequency dependence of the Stokes vectors for a given scattering order. Substituting $\tau = \tau_{\rm T}$ into equation (11) and $\tau = 0$ into equation (12), we obtain the emergent Stokes vectors.

### 3.2. *Radiative Transfer in Cylinders*

In order to treat radiative transfer in cylindrical geometry, we divide the cylinder into horizontal spatial layers and average the computed radiation field over each layer (over the radial and the azimuthal directions), leaving only the dependence on the zenith angle. To simplify the calculations, we assume that the soft (reprocessed and internally produced in the cold disk) and reflected radiation enter uniformly at the base of the cylinder. Thus we effectively convert the two-dimensional problem into a one-dimensional problem.

The boundary conditions are the same as in the slab case, but the radiation incident on the base of the cylinder is now

$$I_{\rm in}(x, \mu) = gI_{\rm refl}(x, \mu) + c_{\rm bb}B_x(T_{\rm bb})(1 \quad 0)^T + c_{\rm disk}B_x(T_{\rm disk})(1 \quad 0)^T\,. \tag{14}$$

The parameter $g$ is the fraction of the reprocessed and reflected radiation from the cold disk that enters the active region. In the case of slab geometry, $g = 1$. For cylinders atop a cold disk, $g \approx 0.6$ if the vertical $\tau_{\rm T}$ equals the radial $\tau_R = Rn_e\sigma_{\rm T}$, while $g \approx 0.45$ for $\tau_{\rm T} = 2\tau_R$. The parameter $g$ is smaller for active regions detached from the cold disk. The normalization constants, $c_{\rm bb}$ and $c_{\rm disk}$, are given by

$$c_{\rm bb}\pi\int_0^\infty dx\,B_x(T_{\rm bb}) = \frac{gl_{\rm repr}}{\pi}\,, \qquad c_{\rm disk}\pi\int_0^\infty dx\,B_x(T_{\rm disk}) = \frac{l_{\rm disk}}{\pi}\,. \tag{15}$$

The expressions that connect the radiation field inside the cylinder with the source function are analogous to equations (11) and (12):

$$I_k^+(\tau, x, \mu) = \int_0^\tau \frac{d\tau'}{\mu}\,S_k(\tau', x, \mu)\exp\left[-\int_{\tau'}^\tau \sigma(\tau'', x, \mu)\frac{d\tau''}{\mu}\right]C_+^{\rm in}(\tau, \tau', \mu)\,, \tag{16}$$

$$I_k^-(\tau, x, \mu) = \int_\tau^{\tau_T} \frac{d\tau'}{\mu} S_k(\tau', x, -\mu) \exp\left[-\int_\tau^{\tau'} \sigma(\tau'', x, -\mu) \frac{d\tau''}{\mu}\right] C_-^{\rm in}(\tau, \tau', \mu) , \tag{17}$$

where the correction factors, $C_\pm^{\rm in}$, reduce the contributions from the source function at $\tau'$ to the radiation field at $\tau$ as compared to the slab case (note that $\mu > 0$):

$$C_\pm^{\rm in}(\tau, \tau', \mu) = \begin{cases} 0 , & \text{if } t \geq 1 , \\ (2/\pi)(\arccos t - t\sqrt{1-t^2}) , & \text{if } t \leq 1 , \end{cases} \tag{18}$$

$$t = \sqrt{1-\mu^2}\, |\tau - \tau'| / (\mu 2\tau_R) . \tag{19}$$

The equation for the source function (eq. [13]) remains unchanged.

The emerging (polarized) flux consists of two parts: first, the radiation emerging through the top and the bottom of the cylinder and, second, the radiation emerging through the vertical surface. The first part can trivially be found from equation (16) by multiplying the emerging intensity with $\mu\pi$ ($\pi$ appears because of the definition of the compactness). The second part is given by

$$F_k^{\rm side,\,+}(x, \mu) = \frac{1}{\tau_R} \int_0^{\tau_T} d\tau \int_0^{\tau} \frac{d\tau'}{\mu} S_k(\tau', x, \mu) \exp\left[-\int_{\tau'}^{\tau} \sigma(\tau'', x, \mu) \frac{d\tau''}{\mu}\right] C_+^{\rm em}(\tau, \tau', \mu) , \tag{20}$$

$$F_k^{\rm side,\,-}(x, \mu) = \frac{1}{\tau_R} \int_0^{\tau_T} d\tau \int_\tau^{\tau_T} \frac{d\tau'}{\mu} S_k(\tau', x, -\mu) \exp\left[-\int_\tau^{\tau'} \sigma(\tau'', x, -\mu) \frac{d\tau''}{\mu}\right] C_-^{\rm em}(\tau, \tau', \mu) , \tag{21}$$

where

$$C_\pm^{\rm em}(\tau, \tau', \mu) = 2\sqrt{1-\mu^2}\sqrt{1-t^2} \qquad (t < 1) \tag{22}$$

and is equal to zero otherwise, $t$ being given by equation (19).

### 3.3. *Radiative Transfer in Hemispheres*

In the case of hemispheric geometry, we average over the horizontal layers just as we did for cylindrical geometry. The incident radiation is given by equations (14) and (15), where the parameter $g \approx 0.7$ for hemispheres atop the cold disk. Equations (16) and (17) connect the radiation field inside the hemisphere with the source function, with correction factors $C_\pm^{\rm in}$ being given by

$$C_+^{\rm in}(\tau, \tau', \mu) = \begin{cases} 0 , & \text{if } t \geq r + r' , \\ 1 , & \text{if } t \leq r' - r , \\ C^{\rm in} , & \text{if } r' - r \leq t \leq r + r' , \end{cases} \tag{23}$$

$$C_-^{\rm in}(\tau, \tau', \mu) = \begin{cases} 0 , & \text{if } t \geq r + r' , \\ (r'/r)^2 , & \text{if } t \leq r - r' , \\ C^{\rm in} , & \text{if } r - r' \leq t \leq r + r' , \end{cases} \tag{24}$$

where

$$t = \sqrt{1-\mu^2}\, |\tau - \tau'| / \mu , \qquad r = \sqrt{\tau_T^2 - \tau^2} , \qquad r' = \sqrt{\tau_T^2 - \tau'^2} ,$$

$$C^{\rm in} = \frac{1}{\pi r^2}\left[r^2\phi_* + r'^2 \cos^{-1}\left(\frac{r'^2 - r^2 + t^2}{2r't}\right) - rt \sin\phi_*\right], \qquad \phi_* = \cos^{-1}\left(\frac{r^2 - r'^2 + t^2}{2rt}\right) . \tag{25}$$

The emerging flux through the base of the hemisphere is $\mu\pi I^-(\tau = 0, x, \mu)$. The flux through the curved hemispheric surface is given by equations (20) and (21), where $C_\pm^{\rm em}$ are (note that $\tau_T = \tau_R$ and $\mu > 0$)

$$C_+^{\rm em}(\tau, \tau', \mu) = \begin{cases} 0 , & \text{if } t \geq r + r' , \\ 2\pi\mu\tau/\tau_T , & \text{if } t \leq r' - r , \\ C_+ , & \text{if } r' - r \leq t \leq r + r' , \end{cases} \tag{26}$$

$$C_-^{\rm em}(\tau, \tau', \mu) = \begin{cases} 0 , & \text{if } t \geq r + r' , \\ 0 , & \text{if } t \leq r - r' , \\ C_- , & \text{if } r - r' \leq t \leq r + r' , \end{cases} \tag{27}$$

$$C_\pm = 2[\pm\mu\phi_\pm\tau/\tau_T + \sqrt{1-\mu^2}\sqrt{1-(\tau/\tau_T)^2}\sin\phi_\pm] ,$$

$$\phi_+ = \begin{cases} \phi_* , & \text{if } \mu \geq \sqrt{1-(\tau/\tau_T)^2} , \\ \min(\pi/2, \phi_*) , & \text{if } \mu < \sqrt{1-(\tau/\tau_T)^2} , \end{cases} \tag{28}$$

$$\phi_- = \phi_* .$$

### 3.4. *Isotropic Source Function Approximation*

In some applications in which high accuracy is not needed and we are not interested in the polarization of the radiation, we can substantially reduce the computing time by assuming that the source function, $S_k(\tau, x, \mu)$, is isotropic and homogeneous for scattering orders $k \geq 2$. The accuracy of this approximation is discussed in § 5.2. This approximation works because, for the optically thin coronae, photons scattered more than a few times are almost isotropic and are distributed almost homogeneously throughout the medium. In this case, the iteration procedure, starting from the second scattering order, can be written as follows:

$$S_{k+1}(x) = x^2 \int_0^\infty \frac{dx_1}{x_1^2} R(x, x_1) J_k(x_1) , \tag{29}$$

$$J_{k+1}(x) = S_{k+1}(x) P_J(x) \qquad (k \geq 1) , \tag{30}$$

where

$$J_k(x) = \frac{1}{\tau_T} \int_0^{\tau_T} d\tau \, \frac{1}{2} \int_{-1}^{1} d\mu I_k(\tau, x, \mu) \tag{31}$$

is the intensity averaged over optical depth and angles and

$$R(x, x_1) = \int_0^1 d\mu \int_0^1 d\mu_1 [R_{11}(x, \mu; x_1, \mu_1) + R_{11}(x, \mu; x_1, -\mu_1)] \tag{32}$$

is the angle-averaged Compton redistribution function. The quantity $P_J(x)$ can be obtained from equations (16) and (17):

$$P_J(x) = \frac{1}{\tau_T} \int_0^{\tau_T} d\tau \, \frac{1}{2} \int_0^1 \frac{d\mu}{\mu} \left\{ \int_0^\tau d\tau' \exp\left[ -\int_{\tau'}^{\tau} \sigma(\tau'', x, \mu) \frac{d\tau''}{\mu} \right] C_+^{\rm in}(\tau, \tau', \mu) + \int_\tau^{\tau_T} d\tau' \exp\left[ -\int_{\tau}^{\tau'} \sigma(\tau'', x, -\mu) \frac{d\tau''}{\mu} \right] C_-^{\rm in}(\tau, \tau', \mu) \right\} . \tag{33}$$

In the case of slab geometry, where $C_\pm^{\rm in} = 1$, and at photon energies, $x < 1$, where pair production is not important and hence $\sigma(\tau, x, \mu) = \sigma_{CS}(x)$, this integral can be computed analytically:

$$P_J(x) = \tau_T \frac{1}{\tau_x} \left\{ 1 - \frac{1}{\tau_x} \left[ \frac{1}{2} - E_3(\tau_x) \right] \right\} , \tag{34}$$

where $\tau_x = \tau_T \sigma_{CS}(x)$ is the frequency-dependent optical depth and $E_3$ is the exponential integral of the third order. For $\tau_x \ll 1$, we have

$$P_J(x) \sim \tau_T \frac{1}{2} \left( -\ln \tau_x + \frac{3}{2} - \gamma_E \right) , \tag{35}$$

where $\gamma_E = 0.577216\ldots$ is Euler's constant.

The emergent fluxes through the top and bottom of the cylinder, and through the base of the hemisphere, and from the slab, can be found from equations (16) and (17), where the source functions, $S_k$, can now be taken out from the integrals. Corresponding $\mu$-dependent multiplicative factors similar to $P_J(x)$ can be computed before the iteration procedure. Similarly, the emergent fluxes through the side of the cylinder and through the curved surface of the hemisphere can be found using equations (20) and (21).

## 4. THE BALANCE EQUATIONS

### 4.1. *Energy Balance*

It is common for problems in which pair production is important that the luminosities appear in the form of dimensionless compactnesses. We define the compactnesses in the following way:

1. For an active region (a coronal cylinder or a coronal hemisphere), a dissipation compactness, $l_{\rm diss} \equiv (L_{\rm diss} H/R^2)(\sigma_T/m_e c^3)$, characterizes the dissipation, with $L_{\rm diss}$ being the power providing uniform heating of the active region, $R$ the radius of the cylinder, and $H$ its height. For hemispheres, we have $H = R$. The soft compactness $l_s \equiv (L_s H/R^2)(\sigma_T/m_e c^3)$ characterizes the soft (reprocessed plus internally dissipated) luminosity from the cold disk entering the active region; $l_c \equiv (L_c H/R^2)(\sigma_T/m_e c^3)$ is the coronal compactness that corresponds to the total luminosity of Compton-scattered radiation and radiation emitted in the corona.

2. For a plane-parallel slab corona, a local dissipation compactness is defined as $l_{\rm diss} \equiv (L_{\rm diss}/H)(\sigma_T/m_e c^3)$, with $L_{\rm diss}$ being the power providing uniform heating of a cubic volume of size $H$ in the slab. Similar definitions hold for $l_s$ and $l_c$.

The soft compactness, $l_s$, consist of two parts, $l_{\rm disk}$ and $g l_{\rm repr}$, where $l_{\rm disk}$ is the compactness of the power that is internally dissipated in the cold disk and that enters the corona and $l_{\rm repr}$ is the compactness of the power reprocessed by the cold disk. The parameter $g$ is the fraction of the radiation reprocessed and reflected from the cold disk that enters the active region. Introducing the parameter $d \equiv l_{\rm disk}/l_{\rm diss}$, we can write the energy balance equation for the cold phase as

$$l_s = g l_{\rm repr} + d l_{\rm diss} . \tag{36}$$

If all power dissipates in the corona, then $d = 0$. The total coronal compactness, $l_c$, is the sum of the compactness dissipated in the corona, $l_{\rm diss}$, and the part of the soft and reflected compactnesses that is scattered in corona:

$$l_c = l_{\rm diss} + p_{\rm sc}(l_s + g l_{\rm refl}) . \tag{37}$$

This equation represents the energy balance of the hot phase (i.e., the corona). Here $p_{\rm sc}$ is the probability of scattering in the corona for disk photons entering the base of the active region ($p_{\rm sc}$ is a geometry-dependent function of $\tau_{\rm T}$), and $l_{\rm refl}$ is the compactness reflected from the cold disk. Introducing the integrated disk albedo, $a$, which is the fraction of the incident luminosity reflected by the cold disk, and the anisotropy parameter, $\eta$, which is the fraction of all coronal radiation (Comptonized, annihilation, bremsstrahlung, and double Compton radiation) that is incident on the cold disk, we can write

$$l_{\rm refl} = a\eta l_c , \qquad l_{\rm repr} = (1 - a)\eta l_c . \tag{38}$$

Equations (36)–(38) can easily be solved for the ratios $l_c/l_{\rm diss}$ and $l_s/l_{\rm diss}$:

$$\frac{l_c}{l_{\rm diss}} = \frac{1 + p_{\rm sc} d}{1 - p_{\rm sc} g\eta} , \tag{39}$$

$$\frac{l_s}{l_{\rm diss}} = \frac{g\eta(1 - a) + d(1 - p_{\rm sc} g\eta a)}{1 - p_{\rm sc} g\eta} . \tag{40}$$

Defining the amplification factor, $A \equiv l_c/l_s$, we obtain

$$A = \frac{1 + p_{\rm sc} d}{g\eta(1 - a) + d(1 - p_{\rm sc} g\eta a)} . \tag{41}$$

If all power dissipates in the corona, we have $A = 1/g\eta(1 - a)$.

We now show how to compute the parameters that enter into the energy balance equations from the solution of radiative transfer. Let us define the partial flux emergent from the corona after $k$ scatterings as (note that $\mu > 0$)

$$F_k^+(x, \mu) = \mu I_k^+(\tau = \tau_{\rm T}, x, \mu) , \qquad F_k^-(x, \mu) = \mu I_k^-(\tau = 0, x, \mu) , \tag{42}$$

for slab geometry. For cylindrical geometry, the expressions are the following:

$$\begin{aligned} F_k^+(x, \mu) &\equiv F_k^{\rm side,\,+}(x, \mu) + \mu\pi I_k^+(\tau = \tau_{\rm T}, x, \mu) , \\ F_k^-(x, \mu) &\equiv F_k^{\rm side,\,-}(x, \mu) + \mu\pi I_k^-(\tau = 0, x, \mu) . \end{aligned} \tag{43}$$

Analogous expressions hold for hemispheric geometry, but the upward flux is just $F_k^+(x, \mu) = F_k^{\rm side,\,+}(x, \mu)$. Let us also define $F_0^{\rm in,\,+}$ as the emergent flux of unscattered soft and reflected radiation entering the corona (note that $F_0^{\rm in,\,-} = 0$). The emergent flux of unscattered radiation emitted in the corona is $F_0^{\pm}$. The total emergent coronal flux is then given by $F_c^{\pm} = F_0^{\pm} + \sum_{k=1}^{\infty} F_k^{\pm}$, and the total emergent flux is $F^{\pm} = F_0^{\rm in,\,\pm} + F_c^{\pm}$. The total reflected radiation can be found by convolving the Green's matrix for Compton reflection with the total flux incident on the cold disk:

$$I_{\rm refl}(x, \mu) = \int_x^{\infty} dx_1 \int_0^1 \frac{d\mu_1}{\mu_1} \mathbf{G}(x, \mu; x_1, \mu_1) F^-(x_1, \mu_1) . \tag{44}$$

The integrated disk albedo, $a$, is the ratio of the reflected flux to the total flux incident on the cold disk:

$$a = \frac{\int_0^{\infty} dx \int_0^1 I_{\rm refl}(x, \mu)\mu\, d\mu}{\int_0^{\infty} dx \int_0^1 F^-(x, \mu) d\mu} . \tag{45}$$

The anisotropy parameter, $\eta$, is given by

$$\eta = \frac{\int_0^{\infty} dx \int_0^1 F_c^-(x, \mu) d\mu}{\int_0^{\infty} dx \int_0^1 [F_c^+(x, \mu) + F_c^-(x, \mu)] d\mu} , \tag{46}$$

and the scattering probability, $p_{\rm sc}$, for slab geometry is given by

$$p_{\rm sc} = 1 - \frac{\int_0^{\infty} dx \int_0^1 F_0^{\rm in,\,+}(x, \mu) d\mu}{\int_0^{\infty} dx \int_0^1 I_{\rm in}(x, \mu)\mu\, d\mu} , \tag{47}$$

with similar expressions for hemispheric and cylindrical geometry (but a factor $\pi$ should then be introduced in the denominator). In the calculations, $d$ is specified and $g$ is determined in advance while $a$, $\eta$, and $p_{\rm sc}$ are calculated from the radiative transfer results by using equations (45)–(47), and the amplification factor, $A$, is given by equation (41).

The sum of $l_{\rm diss}$ and $l_{\rm disk}$ can be written as the sum of the total upward emergent flux and the total downward emergent flux that does not reenter the corona:

$$l_{\rm diss} + l_{\rm disk} = 2\pi \int_0^{\infty} dx \int_0^1 [F^+(x, \mu) + (1 - g)F^-(x, \mu)] d\mu . \tag{48}$$

The actual value of $l_{\rm diss}$ is determined by pair balance but does not influence the energy balance.

### 4.2. *Pair Balance*

For the range of temperatures of interest, $\Theta < 2$, particle-particle and particle-photon pair production is negligible compared to photon-photon pair production. The pair annihilation rate, $\dot{n}_{\rm ann}$ cm$^{-3}$, is uniform throughout the corona, while the pair production rate, $\dot{n}_{\gamma\gamma}(\tau)$ cm$^{-3}$, depends on the radiation field inside the medium, being largest at the center, where the photon density is largest, and smallest at the boundaries. In pair balance, the pair annihilation rate, $\dot{n}_{\rm ann}$, is equal to the volume-averaged pair production rate:

$$\dot{n}_{\rm ann} = \bar{\dot{n}}_{\gamma\gamma} , \tag{49}$$

where

$$\bar{\dot{n}}_{\gamma\gamma} = \begin{cases} \dfrac{1}{\tau_{\rm T}} \displaystyle\int_0^{\tau_{\rm T}} \dot{n}_{\gamma\gamma}(\tau) d\tau , & \text{for slabs and cylinders ,} \\ \dfrac{3}{2\tau_{\rm T}} \displaystyle\int_0^{\tau_{\rm T}} \left[1 - \left(\dfrac{\tau}{\tau_{\rm T}}\right)^2\right] \dot{n}_{\gamma\gamma}(\tau) d\tau , & \text{for hemispheres .} \end{cases} \tag{50}$$

Here the extra factor in the integrand for hemispheres accounts for the decreasing volume of horizontal layers with height. The expressions for $\dot{n}_{\rm ann}$ and $\dot{n}_{\gamma\gamma}(\tau)$ are given in the Appendix (§§ A5 and A6).

### 4.3. *Iteration Procedure*

For a given coronal geometry (slab, cylinder, or hemisphere atop the cold disk) only two parameters, $l_{\rm diss}$ (or, alternatively, $\Theta$) and $T_{\rm bb}$, uniquely specify the simulations if all power is dissipated in the corona ($d = 0$). For $d \neq 0$, two more parameters, $d$ and $T_{\rm disk}$, should be specified. The equilibrium state satisfies the energy and pair balance equations coupled with the radiative transfer. To find the solution, we make use of an iterative procedure. For a given $\Theta$, we compute the Compton redistribution matrix, the cross section, and the coronal emissivities (annihilation and bremsstrahlung) and guess the initial values for $l_{\rm diss}$ and $\tau_{\rm T}$. The reflected spectrum and the pair production absorption coefficient are set to be zero. Initial values for the parameters in the energy balance equations are $a = 0$, $\eta = \frac{1}{2}$, and $p_{\rm sc} = 0$. We also compute the amplification factor, $A$, and the soft compactnesses, $l_{\rm repr}$ and $l_{\rm disk}$. We then normalize the incident blackbody radiation by using equation (6) or (15) and thus obtain the incident spectrum, $I_{\rm in}(x, \mu)$, from equation (4) or (14). Solving the radiative transfer by expansion in scattering orders, we find the radiation field inside the medium, as well as the emergent fluxes. We then compute the rate of pair production and the absorption coefficient, the double Compton emissivity, the reflected spectrum, and the albedo, $a$, the parameters $\eta$ and $p_{\rm sc}$, and the amplification factor, $A$.

By comparing $\bar{\dot{n}}_{\gamma\gamma}$ with $\dot{n}_{\rm ann}$ we calculate a new imposed dissipation compactness, $l_{\rm diss}^{\rm new} = l_{\rm diss}^{\rm old}(\dot{n}_{\rm ann}/\dot{n}_{\gamma\gamma})^{1/2}$. Comparing the calculated amplification factor $A^{\rm new}$ with $A^{\rm old}$, we choose the new optical depth, $\tau_{\rm T}$, to be smaller than the old $\tau_{\rm T}$ if $A^{\rm new} > A^{\rm old}$, and larger if $A^{\rm new} < A^{\rm old}$. The change, $\Delta\tau_{\rm T}$, decreases by a factor of 2 for each iteration when the sign of $\Delta\tau_{\rm T}$ changes. After that, we start the next iteration by again solving the radiative transfer.

The number of iterations needed to achieve an accuracy better than 1% in all equations is $\sim 10$. On a SPARC 20, a typical simulation takes $\sim 5$ minutes for six angular points, seven spatial zones, and 80 frequency points. The isotropic source function approximation (see § 3.4) reduces the computing time for solving the radiative transfer problem by an order of magnitude.

## 5. COMPARISON WITH OTHER CODES

### 5.1. *Comparison with Nonlinear Monte Carlo Results*

We compare our calculations based on the iterative scattering method (ISM) with the corresponding results from using the nonlinear Monte Carlo (NLMC) code by Stern (see Stern et al. 1995a). We made three test runs each for slabs and for hemispheres atop the cold disk. We assume that all power dissipates in the corona ($d = 0$). The parameter $g$ is calculated in the iteration procedure, assuming that only the radiation reprocessed below the base of the active region actually reenters the active region. The results are listed in Table 1 and are shown in Figure 1. We find that, for a given $\Theta$, the optical depth, $\tau_{\rm T}$, is almost the same for both codes, with the largest difference being $\sim 5\%$–$8\%$ at small $\tau_{\rm T}$. The difference in the derived compactnesses, $l_{\rm diss}$, is less than 20% for slab geometry. In the case of hemispheres, $l_{\rm diss}$ differs by 20% at large $\tau_{\rm T}$ and is a factor of 2 smaller at small $\tau_{\rm T}$ as a result of our approximate treatment of the radiative transfer in hemispheres. The procedure of averaging the radiation field over the horizontal layers artificially increases the photon density in the active region, causing pair balance to be reached at smaller compactnesses. For large $\tau_{\rm T}$, the difference is smaller as a result of smaller boundary effects. The differences can also be due to our assumed homogeneity of the corona, rather than using a number of zones as in the NLMC method. As shown in Figure 1, both codes yield quite similar spectral shapes for the emerging radiation for both types of geometries. The differences in $l_{\rm diss}$ can be considered small (at least for the slab case) if we remember that $\Theta$ and $\tau_{\rm T}$ depend rather weakly on $l_{\rm diss}$. Thus, if we fix $l_{\rm diss}$ instead of $\Theta$, the differences in $\Theta$ and $\tau_{\rm T}$ will be $\sim 2\%$.

### 5.2. *The Accuracy of Some Useful Approximations*

A number of approximations can be used to decrease the time needed to compute the redistribution function for Compton scattering. One is the isotropic scattering approximation in the electron rest frame (see eq. [A15] in Appendix § A2). We found that, for the mildly relativistic temperatures considered here, the Comptonization spectra computed in this approximation are very accurate at small energies ($x < \Theta$) but have deficits of photons at higher energies. Solving the pair balance in this approximation yields $l_{\rm diss}$ a factor of 6 larger for large $\tau_{\rm T}$ (small $\Theta$) and a factor of 2 larger at small $\tau_{\rm T}$ (large $\Theta$) (see Table 1, where this approximation is denoted ISOSCAT1).

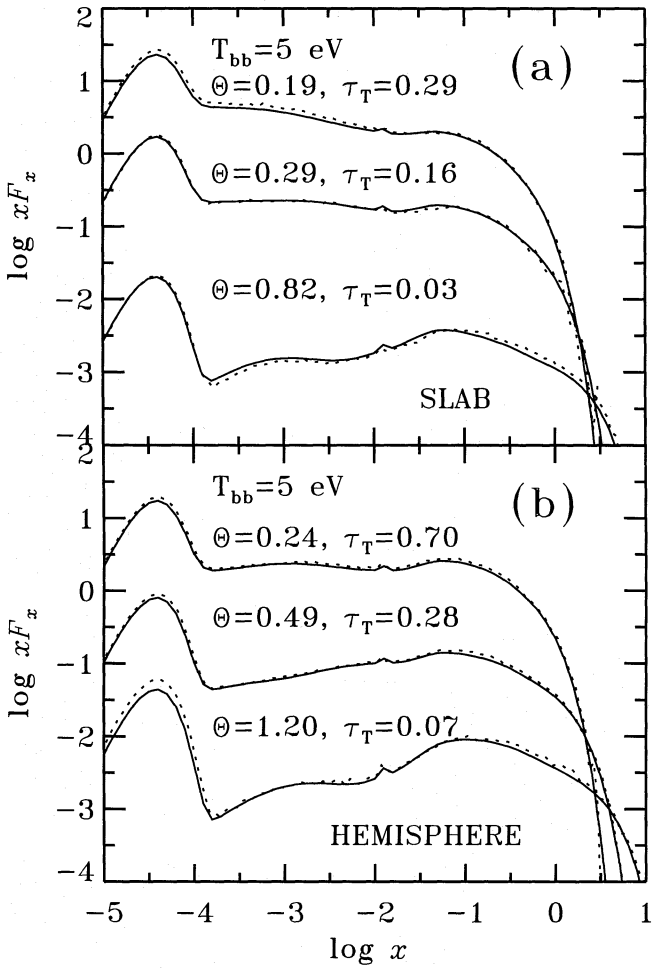


FIG. 1.—(*a*) Emergent flux, $xF_x$ (arbitrary units), from slab pair coronae as function of dimensionless photon energy, $x \equiv h\nu/m_e c^2$, for the parameters in Table 1. The spectra are averaged over viewing angles $0.6 < \mu < 0.9$. Solid and dotted curves illustrate results from the ISM and NLMC codes, respectively. (*b*) Same as (*a*), but for hemispheric coronae.

To improve the high-energy behavior of the Comptonized spectra, we used the redistribution function from equation (A15) and the exact value for $\gamma_*$ from equation (A7). This approximation works much better but still produces a deficit of high-energy photons. We found the resulting $l_{diss}$ to be 10%–30% too large (see Table 1, where this approximation is denoted ISOSCAT2). In Figure 2, spectra in this approximation (*dashed curves*) are compared with exact results (*solid curves*). At low energies ($x < \Theta$), the spectra are almost identical, but the approximate spectra fall more rapidly at larger energies, forcing the compactness to increase in order to satisfy the pair balance. Because of the small contribution of photons with $x \sim 1$ to the total energy balance, the optical depth differs by less than 1% from the exact calculations. We conclude that this approximation is useful for modeling spectra of mildly relativistic pair plasmas.

In many works, the pair production rate is computed by assuming an isotropic radiation field. The isotropic pair production cross section, $R_{\gamma\gamma}^{iso}(xx_1)$ (see Appendix § A8), is much easier to compute than the angle-dependent pair production cross section, $R_{\gamma\gamma}(xx_1, \mu, \mu_1)$ (see, e.g., Coppi & Blandford 1990). In the problem at hand, the radiation field is strongly anisotropic. We investigated the errors caused by making the radiation field isotropic before computing the pair production rate (see Table 1, where this approximation is denoted ISORAD). The resulting $l_{diss}$ are systematically lower than those obtained using the exact angle-dependent $R_{\gamma\gamma}$ because of a higher pair production rate for the isotropic case. The effect is smaller at large $\tau_T$, where the radiation field is more isotropic. Changes in the pair production rate have no influence on the energy balance and consequently do not change the computed spectra and optical depths. They do, however, influence the value of the compactness.

In § 3.4, we presented a method of solving the radiative transfer equation when the source function is assumed to be isotropic starting from the second scattering order. The overall spectral shapes in this approximation (*dotted curves*) are quite similar to the exact spectra (*solid curves*) in Figure 2. The ISOSF approximation underestimates the flux in the "edge on" direction for hemispheric geometry as a result of the artificial isotropization of the radiation field. The differences in optical depth are negligible for slab geometry but become ~3%–10% for hemispheres. The resulting $l_{diss}$ are 10%–50% too large (see Table 1, where this approximation is denoted by ISOSF).

### 5.3. *Comparison with HM93*

In Figure 3, we compare our calculations with the results from Figures 4*a*–4*c* in HM93 for slab geometry. In the low-energy band they are almost identical, but at high energies ($x > \Theta$) the spectra of HM93 have too-sharp cutoffs, reflecting their use of

TABLE 1

COMPARISON OF RESULTS OBTAINED USING THE ISM AND NLMC CODES

| METHOD | SLAB | | | HEMISPHERE | | |
|---|---|---|---|---|---|---|
| | $\Theta$ | $\tau_T$ | $l_{diss}$ | $\Theta$ | $\tau_T$ | $l_{diss}$ |
| ISM | 0.19 | 0.29 | 260 | 0.24 | 0.70 | 560 |
| NLMC | 0.19 | 0.29 | 300 | 0.24 | 0.70 | 700 |
| ISOSCAT1 | 0.19 | 0.29 | 1830 | 0.24 | 0.70 | 2730 |
| ISOSCAT2 | 0.19 | 0.29 | 390 | 0.24 | 0.70 | 740 |
| ISORAD | 0.19 | 0.29 | 250 | 0.24 | 0.70 | 470 |
| ISOSF | 0.19 | 0.30 | 340 | 0.24 | 0.76 | 640 |
| ISM | 0.29 | 0.17 | 19 | 0.49 | 0.29 | 27 |
| NLMC | 0.29 | 0.16 | 20 | 0.49 | 0.28 | 40 |
| ISOSCAT1 | 0.29 | 0.17 | 86 | 0.49 | 0.29 | 70 |
| ISOSCAT2 | 0.29 | 0.17 | 25 | 0.49 | 0.29 | 32 |
| ISORAD | 0.29 | 0.17 | 17 | 0.49 | 0.29 | 20 |
| ISOSF | 0.29 | 0.17 | 23 | 0.49 | 0.30 | 31 |
| ISM | 0.82 | 0.036 | 0.24 | 1.20 | 0.073 | 1.5 |
| NLMC | 0.82 | 0.033 | 0.20 | 1.20 | 0.070 | 3.0 |
| ISOSCAT1 | 0.82 | 0.037 | 0.47 | 1.20 | 0.076 | 2.4 |
| ISOSCAT2 | 0.82 | 0.036 | 0.27 | 1.20 | 0.073 | 1.6 |
| ISORAD | 0.82 | 0.036 | 0.16 | 1.20 | 0.073 | 0.8 |
| ISOSF | 0.82 | 0.036 | 0.27 | 1.20 | 0.075 | 1.6 |

NOTE.—Input parameter: $\Theta \equiv kT_e/m_e c^2$, the dimensionless pair temperature of the corona (volume averaged in the NLMC case); output parameters: $\tau_T$, the (averaged) Thomson optical depth, and $l_{diss} \equiv (L_{diss}/H)(\sigma_T/m_e c^3)$, the local dissipation compactness of the coronal slab or hemisphere. In all cases, $d = 0$ and $T_{bb} = 5$ eV. ISM and NLMC represent results obtained by using the ISM and NLMC codes, respectively. ISOSCAT1 and ISOSCAT2 represent ISM results from using isotropic scattering in the electron rest frame (Appendix § A2). ISORAD represents ISM results when the radiation field is made isotropic before solving the pair balance. ISOSF represents ISM results when the source functions, $S_{k\geq 2}$, are assumed to be isotropic and homogeneous (see § 3.4).

an ad hoc exponential cutoff $\exp(-x/\Theta)$. The actual cutoff energy is approximately $x \approx 2\Theta$, and the cutoff is not a true exponential but rather reflects the thermal Compton scattering kernel and the distribution of the emergent photons over the scattering orders. The spectral indices in the 2–18 keV range, $\alpha_{2-18}$, are very close (see Table 2) for small $\Theta$, but differ at larger $\Theta$. The reason probably lies in the treatment of the reflection from the cold disk. HM93 computed the reflection by using the Monte Carlo method, assuming isotropic incident flux. For large $\Theta$, the *anisotropy break* (see Stern et al. 1995b) occurs in the 2–18 keV range. The flux incident on the cold disk is thus very anisotropic, having its maximum along the normal to the disk. Making the flux isotropic by angle-averaging artificially increases the flux along the plane of the disk, which has a larger probability for reflection (Matt 1993; Poutanen et al. 1996). The contribution of the reflection component to the total flux increases, making the 2–18 keV spectra flatter. This explains the difference in $\alpha_{2-18}$ at large $\Theta$.

TABLE 2

COMPARISON OF ISM RESULTS FOR CORONAL SLABS WITH THOSE OF HM93

| $\Theta$ | $\tau_T$ | $l_{diss}$ | $\alpha_{2-18}$ | | |
|---|---|---|---|---|---|
| | | | $\mu = 0.113$ | $\mu = 0.5$ | $\mu = 0.887$ |
| ISM: | | | | | |
| 0.26 | 0.19 | 34 | 1.15 | 1.11 | 1.08 |
| 0.67 | 0.05 | 0.49 | 0.89 | 0.77 | 0.69 |
| 1.75 | 0.01 | 0.02 | 1.37 | 1.16 | 0.85 |
| $\Theta$ | $\tau_T$ | $l_{diss}$ | $\alpha_{2-18}$ | | |
| | | | $\mu = 0.15$ | $\mu = 0.55$ | $\mu = 0.95$ |
| HM93: | | | | | |
| 0.26 | 0.20 | 22 | 1.23 | 1.14 | 1.10 |
| 0.67 | 0.05 | 2 | 0.87 | 0.73 | 0.65 |
| 1.75 | 0.01 | 0.1 | 1.23 | 0.95 | 0.53 |

NOTE.—Input parameter: $\Theta \equiv kT_e/m_e c^2$, the dimensionless pair temperature of the coronal slab; output parameters: $\tau_T$, the vertical Thomson optical depth of the coronal slab, $l_{diss} \equiv (L_{diss}/H)(\sigma_T/m_e c^3)$, the dissipation compactness of the coronal slab, and $\alpha_{2-18}$, the least-squares fitted 2–18 keV intensity slope for three specified cosine angles. In all cases, $d = 0$ and $T_{bb} = 5$ eV. See text for determination of $l_{diss}$ from HM93.

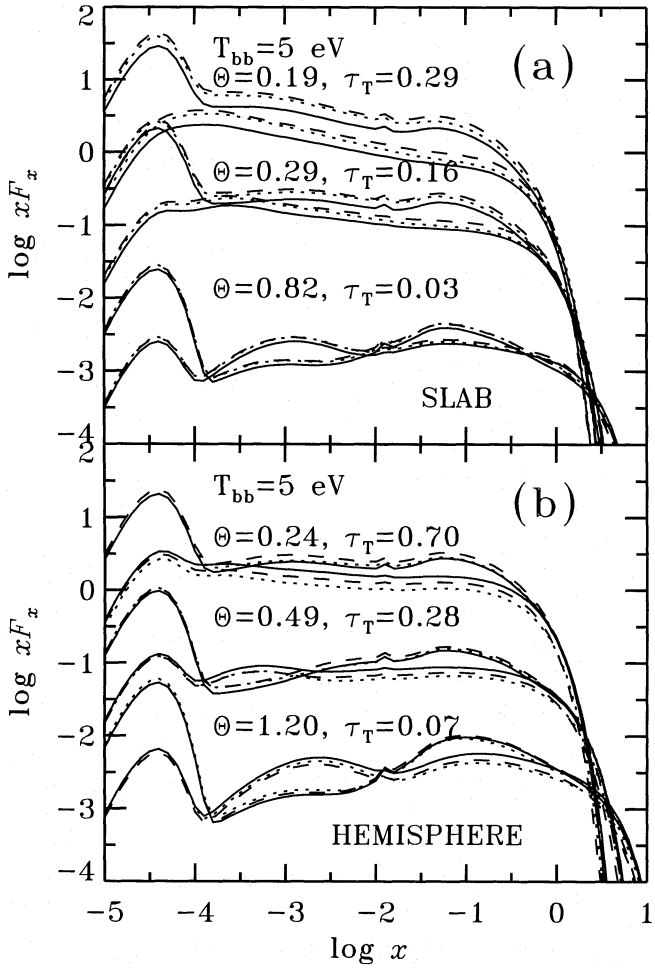


FIG. 2.—Same as Fig. 1, but for two viewing angles, $\mu = 0.11$ and $\mu = 0.89$. The face-on spectra ($\mu = 0.89$) can be identified by their more prominent blackbody component. All curves represent results from the ISM code. Results using the exact scattering kernel are shown by solid curves. Dashed curves represent results assuming isotropic scattering in the electron rest frame (ISOSCAT2, see Appendix § A2). Dotted curves correspond to the isotropic source function approximation (ISOSF). Note that the emergent spectra for the different approximations are normalized to the corresponding value of $l_{\rm diss}$ in Table 1. The spectral fluxes in a given direction differ slightly, but the spectral shapes are almost identical.

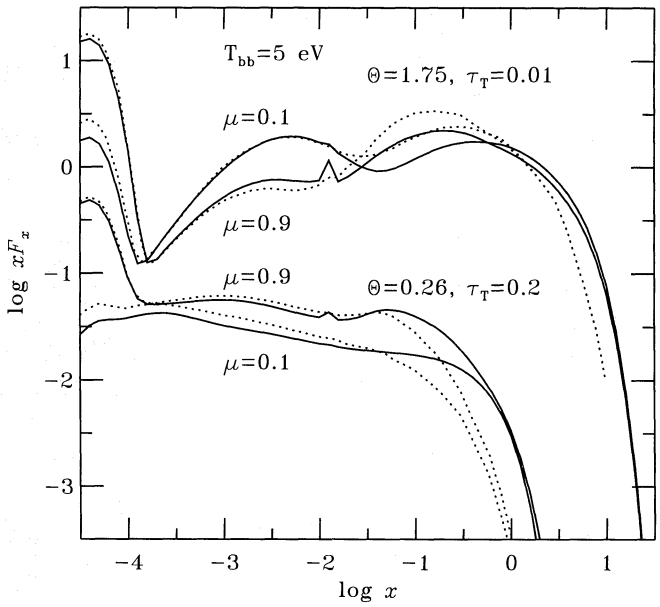


FIG. 3.—Emergent flux, $xF_x$ (arbitrary units), from slab pair coronae as function of dimensionless photon energy, $x \equiv h\nu/m_e c^2$. Solid curves illustrate results from the ISM code for $\mu = 0.11$ and $\mu = 0.89$; dotted curves, results from Figs. 4*a* and 4*c* in HM93 for $\mu = 0.15$ and $\mu = 0.95$.

The $\Theta$-$\tau_T$ relation obtained by our code agrees with calculations of HM93 to within a percent or two for small $\tau_T \approx 0.01$. The difference increases with increasing $\tau_T$, and at our largest $\tau_T$ of 0.37, the $\Theta$ of HM93 is $\sim 10\%$ too large because of our spectral differences and the corresponding influence on the energy balance. The anisotropy factor, $\eta$ (see Fig. 2*a* in HM93), agrees very well up to $\tau_T = 0.1$. Above that, the $\eta$ of HM93 is slightly too small, becoming 0.02 smaller at $\tau_T = 0.37$, most likely as a result of our $\Theta$ being 10% smaller. Our albedo, $a$, is smaller (0.13 instead of 0.16) at small $\tau_T$ (see Fig. 2*b* in HM93). Above $\tau_T = 0.05$, our $a$ is 0.01 larger. The differences are likely a result of our use of a fully relativistic and anisotropic treatment of the reflection.

The comparison of compactnesses is not so easy. First of all, HM93 gave the values for the Compton compactness $l_c$, which is related to the total dissipation compactness as $l_{\rm diss} = (1 - p_{\rm sc}\eta)l_c$, where $p_{\rm sc}$ is the probability of scattering in the corona (see § 4.1). Second, they defined the compactness to be factor of $\pi$ larger than our definition. Thus, in Table 2, we list the corrected $l_{\rm diss} = (1 - p_{\rm sc}\eta)l_c/\pi$ instead of the original values of $l_c$ from Table 1 in HM93. For small $\tau_T$, our compactnesses are a factor of 5 smaller, but for $\tau_T = 0.2$, our compactness is larger than the corresponding compactnesses of HM93. The approximate estimates by HM93 of the pair-producing photon density inside the slab (see Appendix B in HM93) and the prescription for the Comptonized spectra (Zdziarski 1985) used in the pair balance calculations are responsible for the remaining differences.

### 5.4. *Comparison of Comptonized Spectra with Analytic Formulae*

We compare the angle-averaged Comptonized spectra computed by use of the ISM code with the analytic formulae for thermal Comptonization from the papers by Titarchuk (1994, his eqs. [35] and [44]) and Hua & Titarchuk (1995, their eqs. [9] and [10]). We consider monochromatic incident photons with $h\nu_0 = 8$ eV on the lower boundary of the slab. The only process that is taken into account is Comptonization. No pair or energy balance is imposed. Calculations for three different optical depths and temperatures are presented in Figure 4. All three cases correspond to regime 2 in Hua & Titarchuk (1995). We find that the Hua & Titarchuk formulae rather well represent the general spectral behavior but yield systematically fewer photons in the high-energy tail. The Titarchuk formulae, however, provide a very good description of the spectra for relatively small temperatures ($\Theta < 0.2$), while they produce too many photons in the Wien bump for larger temperatures. In all these cases, we should, however, remember that spectra below the anisotropy break, as well as the high-energy tail, have quite different behavior at different viewing angles. The analytic formulae do not provide this angular dependence of the spectrum and are therefore quite limited in practice.

### 5.5. *Polarization Properties*

In this section, we compare our calculations of the degree of polarization of the radiation emerging from the slab-corona with some earlier results by others. We assume here that the cold disk emits semi-isotropic, unpolarized radiation. We define the degree of polarization as $p = (Q/I)100\%$. The polarization is positive when the electric vector is predominantly parallel to the normal to the slab. The behavior of the total polarization is affected by both the Compton scattered radiation from the hot corona and by reflected radiation from the cold disk.

Sunyaev & Titarchuk (1985) calculated the polarization of the Comptonized radiation from a slab. The angular and polarization structure of the radiation field were obtained with an iteration procedure based on an expansion in scattering orders using the Rayleigh matrix. The frequency dependence of the intensity was obtained by solving the Kompaneets

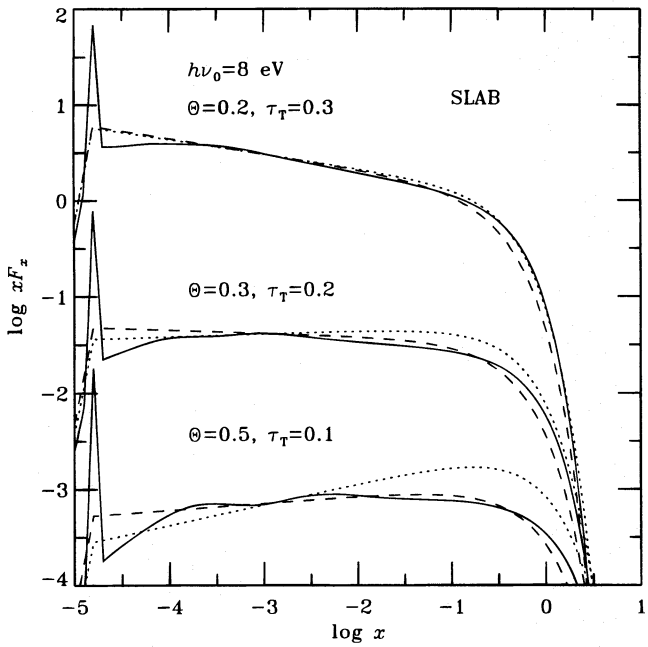


FIG. 4.—Angle-averaged Comptonized spectra, $xF_x$ (arbitrary units), from slab coronae as function of dimensionless photon energy, $x \equiv h\nu/m_e c^2$. Soft monochromatic photons with $h\nu_0 = 8$ eV are assumed to be incident on the lower boundary of the slab. Solid curves illustrate results using the ISM code; dotted curves, spectra using eqs. (35) and (44) from Titarchuk (1994); dashed curves, spectra using eqs. (9) and (10) from Hua & Titarchuk (1995). No pair or energy balance is imposed.

equation (see Sunyaev & Titarchuk 1980), which is a diffusion equation in frequency space. The distribution of photons over escape time and thus the relation between the scattering order and frequency were obtained by solving the diffusion equation in physical space. This approach has a few shortcomings. First, the diffusion approximation in optical depth (i.e., physical space) is not valid for the optically thin coronae considered here. Second, for the case of a hot electron gas, the frequency redistribution cannot be considered as diffusion, because of the large frequency shift in each scattering. And last, for high electron temperatures ($\Theta \gtrsim 0.1$), large photon energy ($x \gtrsim 0.1$), or both, the polarization properties of the exact Compton redistribution matrix are quite different from those of the Rayleigh matrix (Poutanen & Vilhu 1993). Thus, even for quite small electron temperature, $\Theta = 0.11$, and relatively large optical depth, $\tau_T = 0.5$, the maximum polarization of the hard radiation computed by this method is $p \approx 50\%$ (see Fig. 8 in Sunyaev & Titarchuk 1985; note also that their $\tau_0 = \tau_T/2$), compared to $p \approx 25\%$ in our calculations (see our Fig. 5). The differences become much larger for smaller $\tau_T$ and/or larger $\Theta$.

Following the same idea of separating the polarization structure from the frequency redistribution, Haardt & Matt (1993) computed the degree of polarization from an optically thin, hot slab-corona by applying the method of Haardt (1993) to obtain the spectra. Using an iterative scattering scheme similar to ours, they avoided the diffusion approximation both in frequency and optical-depth space. They, however, still used the Rayleigh matrix. To compare the results, we have chosen the same parameters as in Figure 2 in Haardt & Matt (1993). The blackbody temperature is taken to be $T_{bb} = 10$ eV; the optical depth is $\tau_T = 0.5$ and 0.05. We show the results of our computations in Figures 5 and 6. We present the results for two viewing angles, $\mu = 0.11$ and $\mu = 0.50$. The degree of polarization is zero in the direction normal to the slab as a result of symmetry. It is clearly seen that the degree of polarization is much too large in Haardt & Matt (1993). They found the maximum polarization to be $p \approx 45\%$ for $\tau_T = 0.5$ and $p \approx 33\%$ for $\tau_T = 0.05$ while we obtained $p \approx 25\%$ and $p \approx 5\%$, respectively (Figs. 5, 6; *thick solid curves*).

Below we discuss the polarization properties both of the Comptonized radiation from the hot corona and of the radiation reflected from the cold slab. In order to better see the contribution to the overall polarization from different scattering orders, we also show the spectra for individual scattering orders, as well as the total spectrum, in the upper panels of Figures 5 and 6.

First, we consider the polarization caused by scattering in the hot corona. The degree of polarization increases with the number of scatterings, reaching its asymptotic value after few scatterings. The asymptotic value depends on optical depth, temperature, and zenith angle. At energies close to $m_e c^2$, the Klein-Nishina corrections start to be important, decreasing the polarization. As the electron temperature increases, the polarization decreases (Poutanen & Vilhu 1993). At a given frequency, the contribution from the higher scattering orders (with larger polarization) becomes smaller, also decreasing the polarization. For these two reasons, the polarization in Figure 5 ($\tau_T = 0.5$) is larger than in Figure 6 ($\tau_T = 0.05$). The polarization of a given scattering order first decreases toward higher energies but then increases as a result of the contribution from the scattered

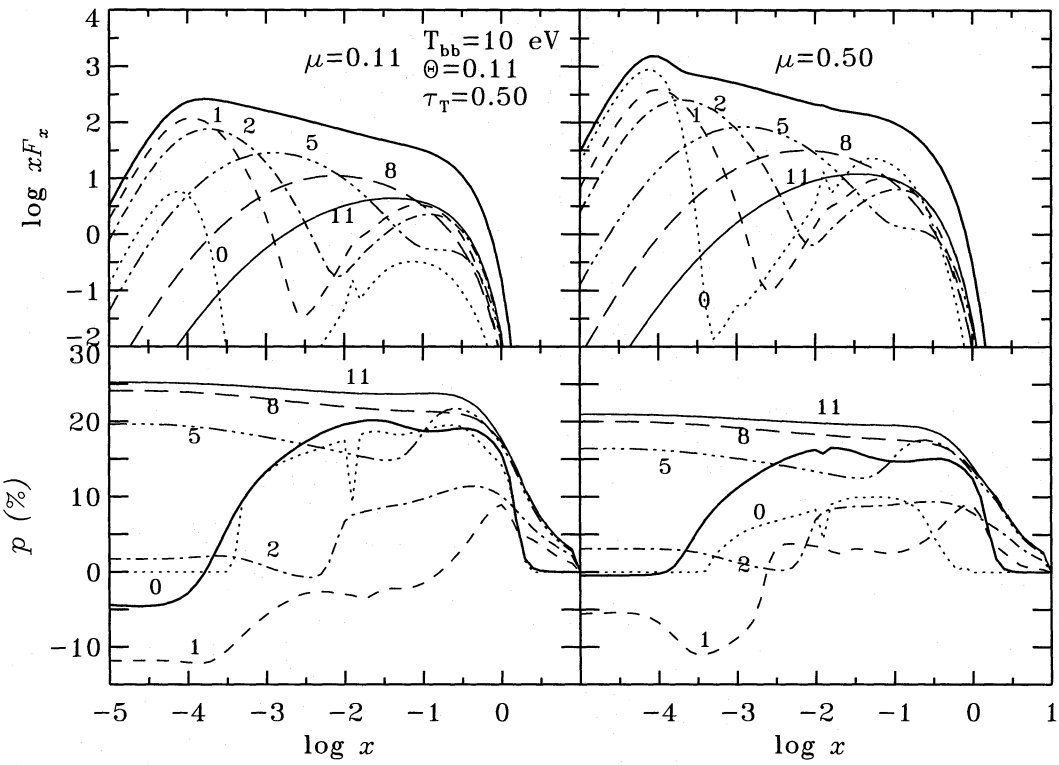


FIG. 5.—Emergent flux, $xF_x$, from slab-coronae (*top*) and the degree of polarization, $p$ (*bottom*) as function of dimensionless photon energy, $x \equiv h\nu/m_e c^2$, for $\Theta = 0.11$, $\tau_T = 0.50$, $T_{bb} = 10$ eV for two viewing angles, $\mu = 0.11$ and $\mu = 0.50$. No pair or energy balance is imposed. Thick solid curves show the overall spectra and polarization. The contribution from some of the scattering orders is also shown. The labels show the order of scattering. The zeroth component (*dotted curves*) consists of the unpolarized blackbody disk radiation, as well as the radiation reflected from the cold disk. The scattered components consist of multiple scattered blackbody radiation and multiple scattered reflected radiation, with the latter being centered around $x \sim 0.1$.

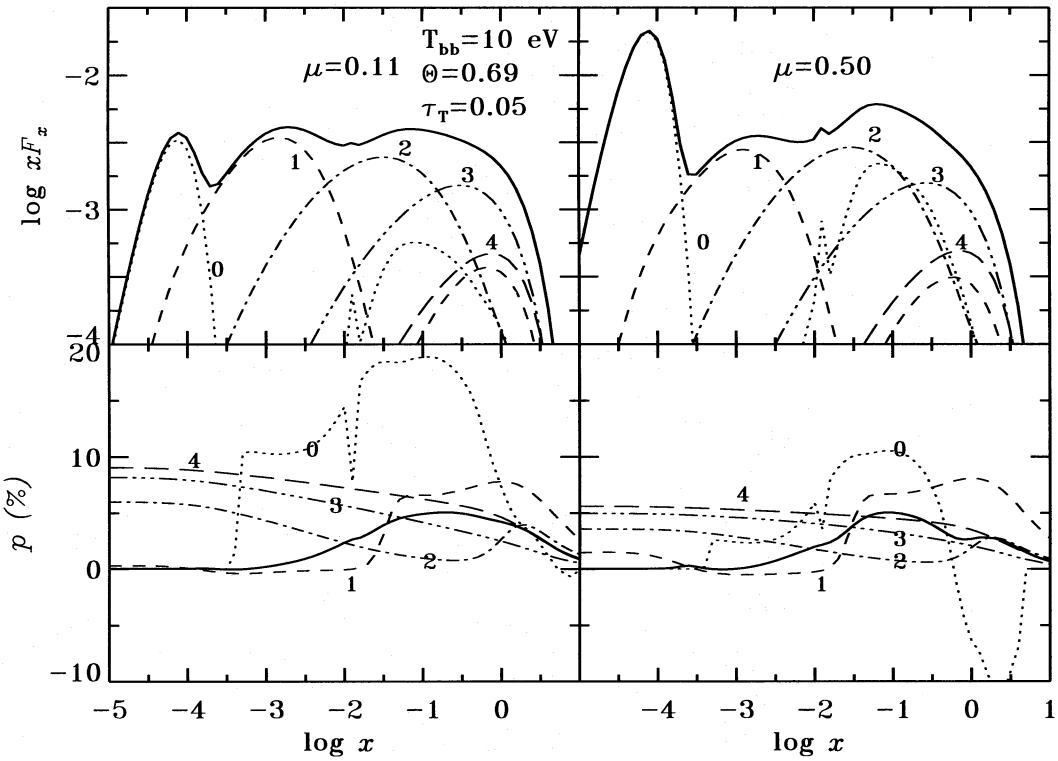


FIG. 6.—Same as Fig. 5, but for $\tau_T = 0.05$ and $\Theta = 0.69$

reflected component. The decrease is caused by the fact that the largest energy shift is obtained in backward scatterings, which do not produce additional polarization.

The reflection component contributes to the overall spectra at energies $x \approx 0.01$–1. When the flux incident on the cold disk is nearly isotropic, which is the case for optically thin coronae, the polarization of the reflected component is positive at $x \lesssim 1$. It is maximal in edge-on directions and is zero in the normal direction (see Poutanen et al. 1996 for a discussion of the polarization properties of Compton-reflected radiation from the cold slab). The polarization in the direction close to the normal decreases at higher energies, changing sign at $x \sim 0.6$. The flux reflected close to the normal direction cuts off at energies above $x \sim 1$. At directions closer to the plane of the slab, the cutoff is slower and is determined by the cutoff of the incident spectrum. The polarization has a sharp feature at 6.4 keV due to the contribution from the unpolarized fluorescent iron line.

For $\tau_T = 0.5$ (Fig. 5), the polarization of the reflected radiation (and that of the reflected component scattered once or twice in the corona) is smaller than the polarization of the component produced by Compton scatterings in the hot corona. This causes the polarization to decrease at $x > 0.1$. On the other hand, for $\tau_T = 0.05$ (Fig. 6), the reflected component has significantly larger polarization than the scattered component, resulting in a smoothly increasing polarization in the energy interval from $x \approx 0.01$ up to $x \sim 0.1$. The decrease of the polarization of the reflected component at higher energies and the change of sign at $x \sim 0.6$ for $\mu = 0.5$ cause the drop in the total polarization at $x \sim 1$.

Future observations of X-ray polarization by the *Spectrum-X-Gamma* satellite (Kaaret et al. 1992) can be a powerful tool for determining the physical conditions and, probably, the geometry of the X-ray–emitting region in AGNs and X-ray binaries. We note here that the degree of polarization for hemispheric and cylindrical geometries is smaller than for the slab case. We can conclude that if small polarization in the X-rays were observed, this could argue for Comptonization models in which the temperature of the electron gas is large and/or for models in which the geometry of the corona is not slablike.

## 6. SUMMARY AND CONCLUSIONS

We have described a versatile code based on the iterative scattering method (ISM) to accurately solve the radiative transfer and Comptonization in a two-phase disk-corona models for active galactic nuclei and X-ray binaries. The code has several attractive features, some of them unique to this code:

1. The radiative transfer is fully angle dependent, and one can easily determine the outgoing spectrum in any direction to high accuracy at any photon energy. The outgoing spectrum in a given direction may differ greatly from the angle-averaged spectrum.
2. The radiative transfer is valid for both nonrelativistic and relativistic temperatures.
3. The radiative transfer is polarized.
4. Most important radiation processes in hot thermal plasmas, including Compton scattering, photon-photon pair production, pair annihilation, bremsstrahlung, and double Compton scattering, are taken into account. The latter two were not important for the parameters of the test cases we considered in this paper.

5. The corona can be in energy balance, pair balance, or both.
6. The corona can either be a pure pair corona, or one can include a background plasma.
7. The reflection by the cold disk is exactly treated by using a reflection matrix that, in particular, accounts for the full angular dependence of the incident radiation.
8. The ISM code has been extensively tested against a nonlinear Monte Carlo (NLMC) code (Stern et al. 1995b), finding very good agreement.
9. The ISM code is an order of magnitude faster than the NLMC code. The ISM code also allows for an easier determination of the spectral falloff at photon energies above $kT_e$. The ISM code also yields more accurate emerging spectra at a given viewing angle as compared to the NLMC code, in which one must average over a range of viewing angles in order to improve the photon statistics.
10. Various approximations for the radiative transfer/Comptonization can be used in order to improve computing efficiency. Quite accurate results can be obtained if one assumes the Compton scattering source function to be isotropic. The gain in computing efficiency is then an order of magnitude. A typical run on a SPARC 20 then takes $\sim$40 s for six angular, 80 frequency, and seven spatial grid points.

There are, however, some limitations:

1. The iterative scattering method converges only for small optical depths. For small temperatures ($\Theta < 0.1$) and large optical depths ($\tau > 1$), the round-off errors become large because of the large number of scatterings, and the accuracy of the results decreases. The maximum allowed $\tau_T$ depends on the temperature and is $\sim$1 for $\Theta = 0.1$ and 1.5 for $\Theta = 0.5$ in the slab case and 2–3 in the case of hemispheric geometry. This is not much of a limitation at temperatures above $\sim$100 keV, as the optical depths needed to explain observed X-ray spectral indices in AGNs are necessarily less than unity.
2. The ISM code is one-dimensional. It can, however, be applied to quasi–one-dimensional radiative transfer in two-dimensional active regions with cylindrical or hemispheric geometry atop or elevated above the cold disk. The NLMC code can, in principle, treat arbitrary geometries.
3. The corona is uniform in temperature and density. The nonlinear Monte Carlo code has been used (Stern et al. 1995b) to show that the differences in temperature and density across the corona amount to at most a factor 2. In principle, one could divide the corona into a few zones and solve the radiative transfer equation by using the appropriate Compton redistribution functions and cross sections corresponding to the temperature in each zone. The pair and energy balance equations should then be solved in each zone separately. This, however, is much more time-consuming than considering a homogeneous corona. The resulting spectra from homogeneous and inhomogeneous coronae are very similar.
4. The ISM code treats steady radiative transfer. The NLMC code, on the other hand, can treat time-dependent situations.

There are several possible applications of the ISM code:

1. Results of earlier work using various approximations can be checked and the validity of the approximations tested. In particular, we find that the full Compton redistribution matrix, rather than the Rayleigh scattering matrix, must be used in order to obtain accurate polarized X-ray spectra.
2. The validity of published analytic fits for angle-averaged Comptonized spectra can be checked. The results of the ISM code can be used to obtain analytic fits of spectra as function of viewing angle and for different geometries.
3. The ISM code has great potential for modeling X-ray and $\gamma$-ray spectra from active galactic nuclei and X-ray binaries. The ISM code has already been used together with an NLMC code to interpret the statistics of observed X-ray spectral indices and compactnesses from Seyfert 1 galaxies (Stern et al. 1995b). The anisotropy of outgoing spectra is an important ingredient in this interpretation, which could not have been done with angle-averaged model spectra.
4. The ISM code is highly suitable for inclusion in spectral fitting software such as XSPEC, whereupon observed X-ray spectra can be modeled. Such modeling of a number of sources will appear in a forthcoming work.
5. The ability of the ISM code to treat polarized radiative transfer makes it a powerful tool for interpreting future observations of X-ray polarization from, e.g., the *Spectrum-X-Gamma* and *International Gamma-Ray Astrophysical Laboratory* satellites.

The authors thank Boris Stern for stimulating discussions. This research was supported by grants and a postdoctoral fellowship (J. P.) from the Swedish Natural Science Research Council.

## APPENDIX

## RATES OF THE PHYSICAL PROCESSES

### A1. THE ELECTRON SCATTERING SOURCE FUNCTION AND THE COMPTON REDISTRIBUTION MATRIX

The thermal electron scattering source function, $S(\tau, x, \mu)$, for an azimuth-independent radiation field, accounting only for linear polarization, can be expressed in terms of the azimuth-averaged Compton redistribution matrix, $\mathbf{R}(x, \mu; x_1, \mu_1)$, as

$$S(\tau, x, \mu) = x^2 \int_0^\infty \frac{dx_1}{x_1^2} \int_{-1}^{1} d\mu_1 \mathbf{R}(x, \mu; x_1, \mu_1) I(\tau, x_1, \mu_1) , \quad \text{(A1)}$$

Here **R** is the azimuth-averaged product of two rotational matrices, **L**, and the thermal Compton redistribution matrix, $\mathbf{C}(x, x_1, \cos\theta)$ (Poutanen & Vilhu 1993):

$$\mathbf{R}(x, \mu; x_1, \mu_1) = \int_0^{2\pi} d\varphi\, \mathbf{L}(-\chi)\mathbf{C}(x, x_1, \cos\theta)\mathbf{L}(\chi_1)\,. \tag{A2}$$

In general, it is 4 × 4 matrix. The rotational matrices are given by the following expression (see, e.g., Chandrasekhar 1960):

$$\mathbf{L}(\chi) = \begin{pmatrix} 1 & 0 & 0 & 0 \\ 0 & \cos 2\chi & \sin 2\chi & 0 \\ 0 & -\sin 2\chi & \cos 2\chi & 0 \\ 0 & 0 & 0 & 1 \end{pmatrix}. \tag{A3}$$

As a result of azimuthal symmetry and the absence of circular polarization, we consider only the 2 × 2 matrix in the upper left corner of the general matrix:

$$\mathbf{R} = \begin{pmatrix} R_{11} & R_{12} \\ R_{21} & R_{22} \end{pmatrix}. \tag{A4}$$

The elements of this matrix are

$$R_{11} = \int C\, d\varphi\,, \qquad R_{12} = \int C_I \cos 2\chi_1\, d\varphi\,,$$
$$R_{21} = \int C_I \cos 2\chi\, d\varphi\,, \qquad R_{22} = \int [C_+ \cos 2(\chi - \chi_1) + C_- \cos 2(\chi + \chi_1)] d\varphi\,, \tag{A5}$$

where $C_\pm = (C_Q \pm C_U)/2$ and the cosines are given by

$$\cos\chi = \frac{\mu_1 - \mu\cos\theta}{\sin\theta\sqrt{1-\mu^2}}\,, \qquad \cos\chi_1 = \frac{\mu - \mu_1\cos\theta}{\sin\theta\sqrt{1-\mu_1^2}}\,, \tag{A6}$$

with $\cos\theta = \mu\mu_1 + (1-\mu^2)^{1/2}(1-\mu_1^2)^{1/2}\cos\varphi$. Finally, the functions $C$, $C_I$, $C_Q$, and $C_U$ are four of the five functions that form the thermal Compton redistribution matrix, $\mathbf{C}(x, x_1, \cos\theta)$. This matrix is given by a single integral over the electron energy distribution, $f(\gamma)$, and the Compton redistribution matrix, $\mathbf{C}^m(x, x_1, \cos\theta, \gamma)$, for an isotropic *monoenergetic* electron gas with Lorentz factor $\gamma$ (Nagirner & Poutanen 1993):

$$\mathbf{C}(x, x_1, \cos\theta) = \begin{pmatrix} C & C_I & 0 & 0 \\ C_I & C_Q & 0 & 0 \\ 0 & 0 & C_U & 0 \\ 0 & 0 & 0 & C_V \end{pmatrix} = \frac{3}{8}\int_{\gamma_*}^{\infty} f(\gamma)\mathbf{C}^m(x, x_1, \cos\theta, \gamma)d\gamma = \frac{3}{8}\int_{\gamma_*}^{\infty} f(\gamma)d\gamma \begin{pmatrix} C_m & C_I^m & 0 & 0 \\ C_I^m & C_Q^m & 0 & 0 \\ 0 & 0 & C_U^m & 0 \\ 0 & 0 & 0 & C_V^m \end{pmatrix}, \tag{A7}$$

where

$$\gamma_* \equiv [x - x_1 + Q(1 + 2/q)^{1/2}]/2\,, \qquad q \equiv xx_1(1 - \cos\theta)\,, \qquad Q^2 \equiv (x - x_1)^2 + 2q\,.$$

The function $C^m$ is the scalar redistribution function derived by Jones (1968; see also Coppi & Blandford 1990). We use the following expressions to calculate the five functions that enter $\mathbf{C}^m(x, x_1, \cos\theta, \gamma)$ in equation (A7):

$$C^m = C_a^m + C_b^m\,, \qquad C_I^m = C_a^m + C_c^m\,, \qquad C_Q^m = C_U^m + C_a^m\,, \qquad C_V^m = C_b^m - qC_a^m\,,$$
$$C_U^m = \frac{2}{Q} + 2\frac{u-Q}{rq}\left[\frac{u-Q}{rq}(2Q+u) - 4\right] + \frac{2u}{vq} + 2R_c^m\,, \tag{A8}$$

where

$$C_a^m = u\frac{(u^2-Q^2)(u^2+5v)}{2q^2v^3} + u\frac{Q^2}{q^2v^2}\,, \qquad C_b^m = \frac{2}{Q} + \frac{u}{v}\left(1 - \frac{2}{q}\right), \qquad C_c^m = \frac{u}{vq}\left(\frac{u^2-Q^2}{rq} - 2\right), \tag{A9}$$

$$u = a_1 - a = (x + x_1)(2\gamma + x_1 - x)/(a + a_1)\,, \qquad v = aa_1\,,$$
$$a^2 = (\gamma - x)^2 + r\,, \qquad a_1^2 = (\gamma + x_1)^2 + r\,, \qquad r = (1 + \cos\theta)/(1 - \cos\theta)\,. \tag{A10}$$

The normalized relativistic Maxwellian distribution is given by

$$f(\gamma) = \frac{e^{-\gamma/\Theta}}{4\pi\Theta K_2(1/\Theta)}\,, \tag{A11}$$

which yields the density of particles in the dimensionless momentum volume, $4\pi z^2\, dz$, normalized to unity. Here $K_n$ is the modified Bessel function of second kind of order $n$, and $z \equiv (\gamma^2 - 1)^{1/2}$. Methods for computing the integrals when averaging

$C^m(x, x_1, \cos\theta, \gamma)$ over a relativistic Maxwellian electron distribution are given in Poutanen (1994). If the electron temperature is not very high ($\Theta < 1$), we can use Gauss-Laguerre quadrature.

### A2. THE COMPTON REDISTRIBUTION FUNCTION FOR ISOTROPIC SCATTERING IN THE ELECTRON REST FRAME

A very simple expression for the redistribution function, $C^m$, can be derived if we assume that the characteristic photon energy in the electron rest frame is small, $x_1\gamma \ll 1$ (i.e., the Thomson limit). The scattering in this limit can be assumed to be coherent in the electron rest frame. We also assume that the scattering is isotropic in the rest frame. Such simplifications yield a correctly normalized redistribution function at energies $x \ll \Theta$ (see eq. [A23]), whose shape slightly differs from the exact one. The function $C^m$ in that approximation becomes (Arutyunyan & Nikogosyan 1980)

$$C^m = 4/(3Q)\,, \tag{A12}$$

being nonzero when

$$2q(\gamma^2 - 1) \geq (x_1 - x)^2\,. \tag{A13}$$

Integration over $\cos\theta$ between the limits defined by equation (A13) yields the angle-averaged redistribution function (Rybicki & Lightman 1979):

$$C^m(x, x_1, \gamma) = \int C^m \sin\theta\, d\theta = \frac{4}{3xx_1}\left(x + x_1 - \frac{\gamma}{z}\,|x - x_1|\right), \tag{A14}$$

where $x/x_1 \in [(\gamma - z)^2, (\gamma + z)^2]$. For Maxwellian electrons, the redistribution function is given by

$$C(x, x_1, \cos\theta) = \frac{1}{8\pi Q}\,\frac{e^{-\gamma_*/\Theta}}{K_2(1/\Theta)}\,, \tag{A15}$$

where $\gamma_* = Q/(2q)^{1/2}$. Equation (A15) is a very good approximation to the exact redistribution function for mildly relativistic temperatures and $x \ll \Theta$. Note also that $xC(x, x_1, \cos\theta)$ is a function of the ratio $x/x_1$. In Table 1, this approximation is called ISOSCAT1. Even better agreement with the exact redistribution function is obtained if $\gamma_*$ from equation (A7) is used in equation (A15). We call this approximation ISOSCAT2 in Table 1. The accuracy of these approximations is discussed in § 5.2.

### A3. THE THERMALLY AVERAGED COMPTON SCATTERING CROSS SECTION

The Compton scattering cross section averaged over a relativistic Maxwellian electron distribution can be written as an integral over the electron energy:

$$\sigma_{\rm CS}(x) = \frac{3\,\sigma_{\rm T}}{16x^2\Theta K_2(1/\Theta)}\int_1^\infty e^{-\gamma/\Theta}\left\{\left(x\gamma + \frac{9}{2} + \frac{2}{x}\,\gamma\right)\ln\left[\frac{1 + 2x(\gamma + z)}{1 + 2x(\gamma - z)}\right] - 2xz\right.$$
$$\left. + z\left(x - \frac{2}{x}\right)\ln(1 + 4x\gamma + 4x^2) + \frac{4x^2z(\gamma + x)}{1 + 4x\gamma + 4x^2} - 2\int_{x(\gamma - z)}^{x(\gamma + z)} \ln(1 + 2\xi)\,\frac{d\xi}{\xi}\right\} d\gamma\,. \tag{A16}$$

Making the substitutions $\gamma = 1 + \Theta \exp(-2t)$ on the interval $[1, 1 + \Theta]$ and $\gamma = 1 + \Theta(1 + t)$ on the interval $[1 + \Theta, \infty)$, and applying a 10-point Gauss-Laguerre quadrature formula, we achieve an accuracy better than 0.02%.

In limiting cases, the thermal cross section can be computed by using simple expressions (Gould 1982; Svensson 1982; Nagirner & Poutanen 1994):

$$\sigma_{\rm CS}(x) = \frac{3\sigma_{\rm T}}{8x^2}\left[4 + \left(x - 2 - \frac{2}{x}\right)\ln(1 + 2x) + \frac{2x^2(1 + x)}{(1 + 2x)^2}\right] \qquad (\Theta \ll 1)\,, \tag{A17}$$

$$\sigma_{\rm CS}(x) = \frac{3\sigma_{\rm T}}{16x\Theta}\left(\frac{1}{2} - \gamma_{\rm E} + \ln 4x\Theta\right) \qquad (\Theta \gg 1,\quad x\Theta \gg 1)\,, \tag{A18}$$

$$\sigma_{\rm CS}(x) = \frac{\sigma_{\rm T}}{K_2(1/\Theta)}\sum_{n=0}^{\infty}(-2x)^n a_n K_{n+2}\left(\frac{1}{\Theta}\right) \qquad (x\Theta \ll 1)\,, \tag{A19}$$

where

$$a_n = \frac{3}{8}\left(n + 2 + \frac{2}{n + 1} + \frac{8}{n + 2} - \frac{16}{n + 3}\right). \tag{A20}$$

These simple approximations can be used to check the correctness of the thermal cross section routine and to estimate the numerical accuracy.

### A4. SYMMETRY PROPERTIES AND A NORMALIZATION CONDITION

The azimuthally and thermally averaged functions $R_{ij}$ have symmetry properties that can be exploited to simplify the radiative transfer equation, to reduce the time needed to calculate all elements of the redistribution matrix, and to check the accuracy of the calculations:

1. *Frequency symmetry.*—

$$R_{ij}(x, \mu; x_1, \mu_1)e^{-x_1/\Theta} = R_{ij}(x_1, \mu; x, \mu_1)e^{-x/\Theta} \qquad (i, j = 1, 2)\,, \tag{A21}$$

which follows from microscopic detailed balance between states $x$ and $x_1$ when the photons and the electrons have a Wien or a Maxwellian distribution, respectively (Pomraning 1973; Mészáros & Bussard 1986). The exponential factors represent the Wien distribution while the photon phase-space factors have been absorbed in the definition of $R_{ij}$.

2. *Angular symmetry.*—

$$R_{ij}(x, \mu; x_1, \mu_1) = R_{ji}(x, \mu_1; x_1, \mu)\,,$$
$$R_{ij}(x, \mu; x_1, \mu_1) = R_{ij}(x, -\mu; x_1, -\mu_1) \qquad (i, j = 1, 2)\,. \tag{A22}$$

These angular symmetries follow directly from the fact that the scattering process depends on the scattering angle between the ingoing and outgoing photons and not on their angle cosines, $\mu$ and $\mu_1$, separately.

The thermal Compton scattering cross section, $\sigma_{\rm CS}(x)$, and the scalar redistribution function, $R_{11}(x_1, \mu_1; x, \mu)$, i.e., element 11 of the thermal redistribution matrix, are related through a normalization condition (see, e.g., Pomraning 1973; Nagirner & Poutanen 1994):

$$\frac{\sigma_{\rm CS}(x)}{\sigma_{\rm T}} = \frac{1}{x}\int_0^\infty x_1\,dx_1 \int_0^1 d\mu \int_0^1 d\mu_1 [R_{11}(x_1, \mu_1; x, \mu) + R_{11}(x_1, \mu_1; x, -\mu)]\,. \tag{A23}$$

Analogous integrations of $R_{12}$ and $R_{21}$ yield zero on the left-hand side as a result of the requirement that the polarization is zero ($Q = 0$) for an isotropic radiation field. These relations can be used to check the accuracy of the calculation of the redistribution matrix and to estimate the quality of the frequency and the angular discretization.

## A5. THE PHOTON-PHOTON PAIR PRODUCTION RATE

For azimuth-independent (i.e., axisymmetric) photon distributions, the rate of photon-photon pair production, $\dot{n}_{\gamma\gamma}$ cm$^{-3}$ s$^{-1}$, neglecting polarization, is given by integrals over dimensionless photon energy, $dx$, and solid angle, $2\pi\,d\mu$, as follows:

$$\dot{n}_{\gamma\gamma}(\tau) = \frac{1}{2}\frac{2\pi}{m_e c^2}\int_0^\infty \frac{dx}{x}\int_{-1}^1 I(\tau, x, \mu)\alpha_{\gamma\gamma}(\tau, x, \mu)d\mu\,. \tag{A24}$$

Here $I(\tau, x, \mu)dx/(cm_e c^2 x)$ is the number density of photons of energy $x$ in the interval $dx$ per steradian traveling in the direction $\mu$ and $\alpha_{\gamma\gamma}$ cm$^{-1}$ is the absorption coefficient due to photon-photon pair production. The factor of $\frac{1}{2}$ is due to both interacting species being photons. The absorption coefficient is given by another integral over the target photon energy, $dx_1$, and solid angle, $d\varphi\,d\mu_1$,

$$\alpha_{\gamma\gamma}(\tau, x, \mu) = \frac{r_e^2}{m_e c^3}\int_0^\infty \frac{dx_1}{x_1}\int_{-1}^1 R_{\gamma\gamma}(x, \mu; x_1, \mu_1)I(\tau, x_1, \mu_1)d\mu_1\,, \tag{A25}$$

where $r_e$ is the classical electron radius, $R_{\gamma\gamma}(x, \mu; x_1, \mu_1)$ is the dimensionless, azimuth-integrated pair production cross section,

$$R_{\gamma\gamma}(x, \mu; x_1, \mu_1) = 2\int_{\varphi_{\rm min}}^\pi s_{\gamma\gamma}(\omega)(1 - \cos\theta)d\varphi\,, \tag{A26}$$

[the $(1 - \cos\theta)$ factor is discussed in, e.g., Weaver 1976], and $s_{\gamma\gamma}(\omega)$ is the dimensionless photon-photon pair production cross section (Jauch & Rohrlich 1976):

$$s_{\gamma\gamma}(\omega) \equiv \frac{\sigma_{\gamma\gamma}(\omega)}{r_e^2} = \frac{\pi}{\omega}\left[\left(2 + \frac{2}{\omega} - \frac{1}{\omega^2}\right)\cosh^{-1}\sqrt{\omega} - \left(1 + \frac{1}{\omega}\right)\sqrt{1 - \frac{1}{\omega}}\right]. \tag{A27}$$

Here $\omega \equiv x_{\rm cm}^2 = xx_1(1 - \cos\theta)/2$, where $x_{\rm cm}$ is the photon energy in the center-of-momentum frame and $\theta$ is the interaction angle, related to other cosines as $\cos\theta = \mu\mu_1 + (1 - \mu^2)^{1/2}(1 - \mu_1^2)^{1/2}\cos\varphi$. Using these relations, the threshold condition for pair production, $x_{\rm cm} > 1$, can be written as a constraint on $\cos\theta$ or on $\cos\varphi$, yielding a minimum allowed value for $\varphi$: $\cos\varphi_{\rm min} = (1 - \mu\mu_1 - 2/xx_1)/[(1 - \mu^2)^{1/2}(1 - \mu_1^2)^{1/2}]$. The factor of 2 in equation (A26) comes from the integration range originally being $\varphi_{\rm min}$ to $2\pi - \varphi_{\rm min}$ and the integrand being an even function of $\varphi$ around $\varphi = \pi$. The axisymmetric pair production rate was previously considered by Stepney & Guilbert (1983), who chose $x_{\rm cm}$ as integration variable instead of $\varphi$. Their rate is a factor of 2 too large, as pointed out by Kusunose (1987).

## A6. THE THERMAL PAIR ANNIHILATION RATE

For a relativistic Maxwellian electron (and positron) distribution, the pair annihilation reaction rate, $\dot{n}_{\rm ann}$ cm$^{-3}$ s$^{-1}$, can be written as a one-parameter ($\Theta$) single integral (Weaver 1976). Svensson (1982) made a simple fit to that integral accurate to within 2%:

$$\dot{n}_{\rm ann} = n_-\,n_+\,cr_e^2\frac{\pi}{1 + 2\Theta^2/\ln(1.3 + 2\eta_{\rm E}\Theta)}\,, \tag{A28}$$

where $\eta_{\rm E} \approx 0.5615$.

### A7. PAIR ANNIHILATION EMISSIVITY

The emissivity due to thermal pair annihilation, $\epsilon_{\rm ann}(x, \Theta)dx$ ergs cm$^{-3}$ s$^{-1}$ sr$^{-1}$, in an energy interval $dx$ can be written by using detailed balance arguments in terms of the pair production cross section in the following form (Svensson 1983):

$$\epsilon_{\rm ann}(x, \Theta) = n_- n_+ r_e^2 m_e c^3 \frac{xe^{-x/\Theta}}{2\pi\Theta K_2^2(1/\Theta)} \int_1^\infty \omega s_{\gamma\gamma}(\omega) e^{-\omega/x\Theta} d\omega \,, \tag{A29}$$

where $s_{\gamma\gamma}(\omega)$ is given by equation (A27). Simple analytic fits for the one-parameter ($x\Theta$) integral in equation (A29) accurate to within 0.04% are given by Svensson, Larsson, & Poutanen (1996).

### A8. SYMMETRY PROPERTIES OF THE AZIMUTH-INTEGRATED PAIR PRODUCTION CROSS SECTION

The azimuth-integrated cross section, $R_{\gamma\gamma}$, obeys energy and angular symmetry relations, which are useful in reducing the computing time:

$$\begin{aligned} R_{\gamma\gamma}(x, \mu; x_1, \mu_1) &= R_{\gamma\gamma}(xx_1, \mu, \mu_1) \,, \\ R_{\gamma\gamma}(x, \mu; x_1, \mu_1) &= R_{\gamma\gamma}(x, \mu_1; x_1, \mu) \,, \\ R_{\gamma\gamma}(x, \mu; x_1, \mu_1) &= R_{\gamma\gamma}(x, -\mu; x_1, -\mu_1) \,. \end{aligned} \tag{A30}$$

These symmetry relations follow directly from equation (A26), the definition of $\omega$, and the relations for $\cos\theta$ and $\cos\varphi_{\rm min}$. To check the accuracy of our calculations, we integrate the azimuth-integrated cross section over one cosine angle and average over the second in order to obtain the fully solid angle–integrated cross section for the isotropic case (which is a well-known function first computed by Gould & Schréder 1967):

$$R_{\gamma\gamma}^{\rm iso}(xx_1) = \frac{1}{2}\int_{-1}^{1} d\mu \int_{-1}^{1} d\mu_1 R_{\gamma\gamma}(x, \mu; x_1, \mu_1) = \int_0^1 d\mu \int_0^1 d\mu_1 [R_{\gamma\gamma}(x, \mu; x_1, \mu_1) + R_{\gamma\gamma}(x, \mu; x_1, -\mu_1)] \,. \tag{A31}$$

Here we have used the third symmetry property above. The angle-averaged function, $\bar{\phi}(xx_1)$ in Gould & Schréder (1967), is related to our $R_{\gamma\gamma}^{\rm iso}(xx_1)$ through $\bar{\phi}(xx_1) = (xx_1)^2 R_{\gamma\gamma}^{\rm iso}(xx_1)/(8\pi^2)$. The angle-averaged cross section, $R(xx_1)$ in Coppi & Blandford (1990), is related to our $R_{\gamma\gamma}^{\rm iso}(xx_1)$ through $R(xx_1) = cr_e^2 R_{\gamma\gamma}^{\rm iso}(xx_1)/(4\pi)$. Coppi & Blandford (1990) gave a useful fit for $R(xx_1)$ accurate to within 7% for all $xx_1$. We find our $R_{\gamma\gamma}^{\rm iso}(xx_1)$ computed by use of equation (A31) to typically be accurate to within 2%.

One can show that the annihilation emissivity can be written as an integral not over the pair production cross section, but over the angle-integrated pair production cross section:

$$\epsilon_{\rm ann}(x, \Theta) = n_- n_+ r_e^2 m_e c^3 \frac{x^3 e^{-x/\Theta}}{16\pi^2\Theta^2 K_2^2(1/\Theta)} \int_0^\infty x_1^2 R_{\gamma\gamma}^{\rm iso}(xx_1) e^{-x_1/\Theta} dx_1 \,. \tag{A32}$$

By numerically computing this integral by use of our computed $R_{\gamma\gamma}^{\rm iso}(xx_1)$ and comparing with equation (A29), we obtain an extra check of the consistency of our pair production and annihilation routines.

### A9. DOUBLE COMPTON EMISSIVITY

The angle-averaged double Compton spectral emissivity, $\epsilon_{\rm DC}(x, \Theta)dx$ ergs cm$^{-3}$ s$^{-1}$ sr$^{-1}$, in an energy interval $dx$ is given by the expression (see, e.g., Svensson 1984)

$$\epsilon_{\rm DC}(x, \Theta) = (n_+ + n_-)x \frac{e^{-x/\Theta}}{2K_2(1/\Theta)} \int_0^\infty x_1^{-3} J(x_1) dx_1 \int_0^\infty \omega \frac{d\sigma_{\rm DC}}{dx}(x, \omega) \exp\left(-\frac{\omega/x_1 + x_1/\omega}{2\Theta}\right) d\omega \,. \tag{A33}$$

Here $J(x_1)$ is the mean intensity of the interacting photons. The differential cross section for the double Compton process is given in Svensson (1984, eqs. [A5], [A6]). In order to account for the high-energy cutoff at $x > \Theta$, we introduced an ad hoc exponential factor, $e^{-x/\Theta}$.

### A10. BREMSSTRAHLUNG EMISSIVITY

The emissivities due to relativistic electron-electron and positron-positron thermal bremsstrahlung, $\epsilon_{\pm\pm}(x, \Theta)dx$ ergs cm$^{-3}$ s$^{-1}$ sr$^{-1}$, in an energy interval $dx$ are given by the expression

$$\epsilon_{\pm\pm}(x, \Theta) = n_\pm n_\pm \sigma_{\rm T} \alpha_f m_e c^3 e^{-x/\Theta} \Theta^{-1/2} \frac{2^{3/2}}{3\pi} g_{\pm\pm}(x, \Theta) \,. \tag{A34}$$

A similar expression holds for the electron-positron emissivity $\epsilon_{+-}(x, \Theta)$. We used the approximations by Skibo et al. (1995) for the Gaunt factors $g_{\pm\pm}(x, \Theta)$ and $g_{+-}(x, \Theta)$. Note that the term of unity in equations (A7), (A9), and (A13) in Skibo et al. (1995) should be deleted.

### A11. NUMERICAL INTEGRATION

All azimuthal integrations are accomplished by use of an 11-point Simpson quadrature. Furthermore, we apply three-point Gaussian quadrature to calculate integrals over zenith angles for each hemisphere. The integration over frequencies is

performed by using rectangular quadrature on a logarithmic frequency scale, $dx/x = d\ln x$, with bin width $\sim 0.1$. The integrals over optical depth are calculated by using rectangular quadrature. The number of points, $N_\tau$, is dependent on the geometry and the optical depth. We typically used $N_\tau = 6$ for slabs and $N_\tau = 11$–21 for active regions.

## REFERENCES


Antonucci, R. 1993, ARA&A, 31, 473
Arutyunyan, G. A., & Nikogosyan, A. G. 1980, Sov. Phys.–Doklady, 25, 918
Chandrasekhar, S. 1960, Radiative Transfer (New York: Dover)
Coppi, P. S., & Blandford, R. D. 1990, MNRAS, 245, 453
Done, C., Mulchaey, J. S., Mushotzky, R. F., & Arnaud, K. A. 1992, ApJ, 395, 275
Gilfanov, M., et al. 1994, ApJS, 92, 411
Gould, R. J. 1982, ApJ, 254, 755
Gould, R. J., & Schréder, G. P. 1967, Phys. Rev., 155, 1404
Haardt, F. 1993, ApJ, 413, 680
———. 1994, Ph.D. thesis, SISSA, Trieste
Haardt, F., & Maraschi, L. 1991, ApJ, 380, L51
———. 1993, ApJ, 413, 507 (HM93)
Haardt, F., Maraschi, L., & Ghisellini, G. 1994, ApJ, 432, L95
Haardt, F., & Matt, G. 1993, MNRAS, 261, 346
Hua, X.-M., & Titarchuk, L. 1995, ApJ, 449, 188
Jauch, J. M., & Rohrlich, F. 1976, The Theory of Photons and Electrons (2d ed.; New York: Springer)
Jones, F. C. 1968, Phys. Rev., 167, 1159
Kaaret, P., et al. 1992, Columbia Astrophys. Lab. Contrib., No. 469
Kusunose, M. 1987, ApJ, 321, 186
Madejski, G. M., et al. 1995, ApJ, 438, 672
Magdziarz, P., & Zdziarski, A. A. 1995, MNRAS, 273, 837
Matt, G. 1993, MNRAS, 260, 663
Mészáros, P., & Bussard, R. W. 1986, ApJ, 306, 238
Mushotzky, R. F., Done, C., & Pounds, K. A. 1993, ARA&A, 31, 717
Nagirner, D. I., & Poutanen, J. 1993, A&A, 275, 325
———. 1994, in Astrophys. & Space Phys. Rev., Vol. 9, Part 1, Single Compton Scattering, ed. R. A. Sunyaev (New York: Harwood), 1
Nandra, K., & Pounds, K. A. 1994, MNRAS, 268, 405
Phillips, K. C., & Mészáros, P. 1986, ApJ, 310, 284
Pietrini, P., & Krolik, J. H. 1995, ApJ, 447, 526
Pomraning, G. S. 1973, The Equations of Radiation Hydrodynamics (Oxford: Pergamon)
Poutanen, J. 1994, J. Quant. Spectrosc. Radiat. Transfer, 51, 813
Poutanen, J., Nagendra, K. N., & Svensson, R. 1996, MNRAS, in press
Poutanen, J., & Vilhu, O. 1993, A&A, 275, 337
Rybicki, G. B., & Lightman, A. P. 1979, Radiative Processes in Astrophysics (New York: Wiley)
Skibo, J. G., Dermer, C. D., Ramaty, R., & McKinley, J. M. 1995, ApJ, 446, 86
Stepney, S., & Guilbert, P. W. 1983, MNRAS, 204, 1269
Stern, B. E., Begelman, M. C., Sikora, M., & Svensson, R. 1995a, MNRAS, 272, 291
Stern, B. E., Poutanen, J., Svensson, R., Sikora, M., & Begelman, M. C. 1995b, ApJ, 449, L13
Sunyaev, R. A., & Titarchuk, L. G. 1980, A&A, 86, 121
———. 1985, A&A, 143, 374
Svensson, R. 1982, ApJ, 258, 321
———. 1983, ApJ, 270, 300
———. 1984, MNRAS, 209, 175
Svensson, R., Larsson, S., & Poutanen, J. 1996, A&AS, in press
Tanaka, Y., & Lewin, W. H. G. 1995, in X-Ray Binaries, ed. W. H. G. Lewin, J. van Paradijs, & E. P. J. van den Heuvel (Cambridge: Cambridge Univ. Press), 126
Titarchuk, L. 1994, ApJ, 434, 570
Weaver, T. A. 1976, Phys. Rev. A, 13, 1563
White, T. R., Lightman, A. P., & Zdziarski, A. A. 1988, ApJ, 331, 939
Zdziarski, A. A. 1985, ApJ, 289, 514
Zdziarski, A. A., Fabian, A. C., Nandra, K., Celotti, A., Rees, M. J., Done, C., Coppi, P. S., & Madejski, G. M. 1994, MNRAS, 269, L55
Zdziarski, A. A., Johnson, W. N., Done, C., Smith, D., & McNaron-Brown, K. 1995, ApJ, 438, L63